# The austenite/martensite interface structure, athermal interface motion, and transformation strain revealed by simulation and theory

F. Maresca* and W. A. Curtin

Institute of Mechanical Engineering, École Polytechnique Fédérale de Lausanne, Lausanne CH-1015, Switzerland

## Abstract

The austenite/martensite (fcc/bcc) interface is prevalent across many new classes of high-strength steels, and yet both its fundamental structure and its mechanism of motion remain uncertain in spite of decades of research. Here, atomistic simulations are used to create an fcc-bcc iron interface having a structure and motion that completely match experimental observations. The simulated interface reveals a defect structure and a mechanism of glissile and athermal propagation that differ in important respects from longstanding assumptions. The atomistically-observed interface defects provide a basis for a parameter-free predictive crystallographic double-shear theory of lath martensite. Predictions of the theory match simulations well and yield very good agreement with experiments on Fe-Ni-Mn and Fe-C. The theory shows that the fcc/bcc lattice parameter ratio is the dominant factor for controlling the transformation strain, which is related to macroscopic toughening, and quantitatively rationalizes many experimental observations. This new understanding about the nature of this special interface provides fundamental insights needed for guiding design of emerging high-strength steels.

## 1. Introduction

The new generation of steels (Quenched and Partitioned[1], Transformation-Induced Plasticity (TRIP)[2,3], bainitic[4] and nanobainitic[5] steels) have high strength and high toughness, and at low cost. They are all multiphase materials consisting of face-centered-cubic (fcc) austenite and body-centered-cubic (bcc) martensite[1-3] or ferrite[4,5]. Many involve a bcc lath martensite structure, so that the dominant austenite/martensite or austenite/ferrite interface has a very special crystallographic orientation. Creation of these steels involves nucleation and growth of the bcc phase from the fcc phase. Performance of these steels requires control of the lath structure (sizes, spacings, variant selection[6,7]) and the phase transformation. The structure and motion of the special fcc/bcc interface are thus essential to both fabrication and performance of these materials. A fundamental understanding of this fcc/bcc interface and the phase transformation is therefore crucial for the design of emerging tough damage-tolerant steels, yet the structure and mechanism of (athermal) motion remain uncertain in spite of decades of research.

Due to its importance, there is a long history of experiment and theory on the austenite/martensite interface. HRTEM studies, as shown in Figures 1a,b, show the main features characterizing the interfacial defect structure in Fe-C (<0.6 wt % C) and Fe-Ni-Mn alloys[4,8-13] to be that

(i) the crystallographic $(111)_{fcc}$ and $(011)_{bcc}$ planes are parallel, denoted $(111)_{fcc} \parallel (011)_{bcc}$, with the macroscopic average interface orientation (the habit plane) being approximately $(xyx)_{fcc}$ with a typical misorientation of $10° < \theta < 20°$ about the $[\bar{1}01]_{fcc}$ direction (Figure 4a), thus lying between $(575)_{fcc}$ and $(121)_{fcc}$. This leads to a stepped interface[4,13], with step direction in Fe-Ni-Mn always close to $[\bar{1}01]_{fcc}$, and step heights being a multiple of the $(111)_{fcc}$ interplanar spacing (see Figure 1); and

(ii) the $[\bar{1}01]_{fcc}$ and $[\bar{1}\bar{1}1]_{bcc}$ closed packed directions are also misoriented by an angle $0° < \varphi < 5.26°$ around the $[111]_{fcc}$ axis, as indicated in Figure 2c. This orientation is between the Kurdjumov-Sachs (KS, $\varphi = 0°$) and Nishiyama-Wassermann (NW, $\varphi = 5.26°$) orientation relationships. Associated with this misorientation is a set of interfacial defects having Burgers vector $a_{bcc}/2\ [1\bar{1}1]$ [4,9].

A convenient way to visualize the deformations required to related fcc and bcc structures is to follow the "Bain path" shown in Figure 2.

The transformation strain is not accurately established; experiments only indicate a strain larger than 0.3[14]. The intrinsic fcc-bcc interface motion occurs with no diffusion and propagates at high speed, i.e the interface is both *glissile* (i.e. it can glide in a conservative manner) and *athermal* (i.e. there is no apparent activation barrier for motion). The structure and motion are essentially independent of temperature[15,16]. This is true even when the macroscopic behavior appears thermally-activated ("isothermal"), which is due to either nucleation or extrinsic interactions with dislocations in the deformed matrix[15,16]. The atomic mechanism of motion has never been observed.

In the long history of this topic, researchers have attempted to rationalize experimental observations of the interface structure and defects, to understand the mechanism of motion, and to determine the transformation strain by experimental analyses[4,8,9], by theories such as the Phenomenological Theory of Martensite Crystallography (PTMC[17-19]) and the Topological Model (TM[20,21]), and by atomistic simulations[22-24]. In spite of significant efforts, there is not yet any complete and predictive understanding of the interface structure, defects, motion, or transformation strain.

The phenomenological PTMC theory for the crystallography, transformation

deformation, and interface structure has been used for over sixty years[15,16,25-27]. The bcc phase takes the shape of a thin plate so as to minimize the elastic energy due to the transformation strain[15,16,25-27]. The theory then searches for candidate interface defects and their glide planes that can predict the observed habit plane, the transformation strain, and the orientation relationship[17-19]. In PTMC, the interface misfit strains are relieved on average at the interface, but there is usually no microscopic model of the interface (see, however, Ref. 17). This yields considerable flexibility, and hence all theories predict a habit plane between $(575)_{\mathrm{fcc}}$ and $(232)_{\mathrm{fcc}}$, consistent with experiments[17-19]. However, the predicted transformation strain and other features vary widely depending on the assumed defects and slip planes. Equally importantly, the assumed defect structures do not clearly predict a glissile or athermal interface[4,28], and so candidate defects must be separately analyzed to assess the prospects for glissile interface motion.

The Topological Model[21] was introduced to study generalized interfaces, and has been applied to the bcc-fcc interface in iron[20]. The model searches for a local periodic unit of coherent terraces defined by arrays of crystallographically-possible lattice dislocations and transformation dislocations (steps/disconnections with Burgers vector content) that can accommodate the interface misfit strains across the interface within each periodic unit. For bcc-fcc iron, the analysis is performed for $(111)_{\mathrm{fcc}} \parallel (011)_{\mathrm{bcc}}$ and within the experimental range of $\varphi$. Various sets of defects are identified, and the combination of a lattice dislocation in bcc and a transformation dislocation is expected to ensure a glissile interface. Application to fcc-bcc ferrous alloys is limited[20] and the existing preliminary predictions are not in detailed quantitative agreement with experiments. In particular, the predicted step direction varies widely (-10° to +6° away from $[\bar{1}01]_{\mathrm{fcc}}$) for $0° < \varphi < 5.26°$, in contrast to experiments on Fe-Ni-Mn. Qualitative comparison with experimental defects in Fe-Ni-Mn was thus achieved only

for one specific orientation relationship $\varphi = 2.76°$ that is ~1° from the average orientation in these materials[4,8]. This is also not consistent with experiments[8,10], which show that the orientation relationship $\varphi$ can vary from KS to NW within the same material. The model makes no statement about whether the interface is athermal since it is based solely on crystallography. Finally, no estimates of the martensitic transformation strain have been made; a small strain approach is proposed in Ref. 21 but may not be adequate for describing the large strains (above 30%).

Atomistic simulations (see also Appendix B) were used mainly to clarify the mechanism of interface motion. However, existing works are all based on EAM-type interatomic potentials that are generally inadequate to study this problem because they are fitted only to bcc properties and are not transferable to fcc. All main fcc properties (lattice parameters, elastic constants, generalized stacking fault energy), as well as the fcc to bcc driving force (see Appendix B and C) are inaccurate or incorrect. Furthermore, there were no clear attempts to obtain an interface structure which matches HRTEM micrographs[4,13]. Specifically, the interfaces considered were (flat) epitaxially semi-coherent[16], thus requiring non-conservative thermally-activated climb to move, inconsistent with experiments. None of the atomistic studies presents any careful analysis of interface defects (Burgers vectors, slip planes and direction), nor any attempt to rationalize the observed results within the crystallographic theory. Finally, no information on the transformation strain has been provided in any atomistic studies.

In this work, we use an appropriate atomistic model and a thorough crystallographic analysis guided by the simulations to develop a new predictive crystallographic theory for the fcc to bcc transformation in iron. Atomistic interfaces for a range of $\varphi$ are constructed guided by the robust observation that the step direction is always close to $[\bar{1}01]_{fcc}$. We then observe the structure and defects that generate the interface, and show very good agreement with experiments[4,8,9]. The atomistic interfaces

are then demonstrated to be both glissile and athermal, consistent with experiments. We then develop a predictive PTMC-type model using the observed defects, which has flexibility to predict many experimental details. We emphasize now that the new crystallographic theory uses insights from the simulations (the set of interface defects), but that the theory is entirely independent of the simulations, just like any other crystallographic theory of martensite transformation. Predictions match simulations well and, moreover, are in good quantitative agreement with experiments. The theory also rationalizes a range of other experimental observations. Overall, the atomistic fcc-bcc iron interface structure and associated crystallographic theory not only agree with experiments but reveal new features and resolve many of the open questions about the structure and mobility of the austenite/martensite interface. The new and physically consistent model of this singularly important material interface can now serve as the basis for guiding development of alloys and microstructures with both high strength and toughness.

The remainder of this paper is organized as follows. Section 2 presents details about the atomistic simulations including validation of the interatomic potential. Section 3 shows the resulting simulation interfaces and identification of the interface defects for the range of orientations between KS and NW, showing full consistency with TEM experiments. Section 4 shows that the simulation interfaces are glissile/athermal, and provides details of the interface motion. Section 5 presents the new crystallographic theory, and shows the perfect match of theory and simulations. Section 6 presents application of the predictive theory to real steels (Fe-Ni-Mn and Fe-C) where the fcc-bcc interface is observed, showing the theory is able to predict all experimental information. Section 7 discusses the implications of the theory for alloy design and for modeling of these steels. Section 8 discusses the theory in the context of the existing PTMC and TM literature. We summarize our findings in Section 9.

## 2. Atomistic simulation details

Here, we construct atomistic Fe fcc-bcc bicrystals in accordance with the macroscopic experimental observations, followed by full atomic relaxation to obtain final microscopic structures. The detailed construction of the interfaces are given in Appendix D. Of most importance is that we impose a step direction in $[\bar{1}01]_{fcc}$ and use periodic unit cells, and these constraints induce some elastic distortions at the interface and can influence the observed structure as discussed below. All simulations are executed using the LAMMPS package[29].

We use the MEAM-T potential[30] for Fe, a second-nearest-neighbor formulation, that captures crucial properties of both fcc and bcc phases (See Appendix C). In particular, at zero pressure and T=0K, the fcc phase enthalpy is +8.5 meV per atom higher than the bcc phase, so that bcc is absolutely stable. With increasing temperature, the fcc-bcc difference in Gibbs free energy decreases to ~3 meV at 600K. The driving force for the fcc to bcc transformation is thus realistic for this potential. With increasing pressure, the enthalpy difference between fcc and bcc also decreases, and fcc becomes more stable than bcc at pressures above 18 GPa at T=0K, in qualitative agreement with experiments. The stability of pure fcc Fe is due to a stable stacking fault energy (SFE) along $[11\bar{2}]_{fcc}$ of +35.7 mJ/m$^2$, which is consistent with paramagnetic DFT computations that predict ~20 mJ/m$^2$ at room temperature[31,32] and consistent with the experimental observations of stable austenite in low-C Fe-C steels (<0.6 wt% C) and Fe-Ni-Mn steels. The fcc and bcc lattice parameters and bcc elastic constants match experiments well. The fcc elastic constants compare well with those obtained via the analytical bond order potential by Müller et al.[33]. The potential also predicts reasonable structures (cores and dissociation distances) for the fcc screw dislocation and the bcc edge dislocations.

We have further validated the potential with respect to recent DFT calculations of

the bcc-fcc interface[34] in the KS orientation relationship $\varphi = 0°$. This interface is not relevant experimentally, and the computationally tractable DFT cell for $\varphi = 0°$ is small and imposes constraints, but is perfectly suitable for validation of the potential. We have reproduced the small periodic simulation cell geometry of the DFT computations and used the MEAM-T potential to compute the relaxed structure of the interface at zero pressure, precisely as done in the DFT study. Figure 3 shows a superposition of the atomic DFT and MEAM-T interface structures; the two DFT structures corresponding to different assumed magnetic distributions in the fcc phase. Agreement between MEAM-T and DFT is excellent; the very small mismatches in exact atomic positions are due to differences in lattice parameter ratio and elastic constants between MEAM-T and DFT, as well as local fluctuations due to the local magnetic environments (not accounted for in MEAM-T). The interface energy predicted by the MEAM-T is 390 mJ/m$^2$, very close to the DFT values (410 mJ/m$^2$ for AFMD and 450 mJ/m$^2$ for SQS magnetic configurations). This level of agreement for an actual DFT-computed fcc/bcc interface (although not one relevant to experiments) further establishes the validity of this Fe MEAM-T potential for studying this class of interfaces in Fe.

## 3. Interface structure and defects: simulation and experiments

Atomistic interfaces have been constructed for $\varphi = 3.11°, 4.75°, 5.21°, 5.7°$, all within, or close to, the experimental range (see Appendix D). Figure 4 compares the atomistic interface for $\varphi = 4.75°$ to the experimentally-observed interface in Fe-Ni-Mn for $\varphi = 3.7°$ [4]; the agreement in atomic positions is remarkable. Differences between simulation and experiments (e.g. the interface plane) are due to differences in $\varphi$ and fcc-bcc lattice parameter ratio (see Tables 1 and 2 discussed later, as well as Appendix D). In Figure 4a, interface steps with heights equal to and larger than one $(111)_{fcc}$

interplanar spacing are visible, consistent with HRTEM experiments[4,13] (see Fig. 1). The interface steps are aligned with $[\bar{1}01]_{fcc}$ with spacing ~1.45 nm close to experiments[4] and to previous predictions[17] (1.33 nm). Note that the use of Common Neighbor Analysis for visualization in Figure 4 and subsequent Figures is imprecise for discerning the local structure and defects.

Figures 5a,b,c show the 3D view of the interface and its defect structure, and Figure 6a shows the structure of the interface on the $(111)_{fcc} \parallel (011)_{bcc}$ plane. Two sets of defects are evident. First, screw dislocations exist with Burgers vector $a_{fcc}/2\,[\bar{1}01]$ lying next to the steps along $[\bar{1}01]_{fcc}$, with the stacking fault between partials lying on the $(111)_{fcc}$ ledge*; these dislocations have never been observed but were assumed to exist*[17]. There is one screw dislocation per step, independent of step height, which was not previously envisioned. The screw dislocations gliding in fcc carry the transformation because they shift atomic positions along $[\bar{1}01]_{fcc}$ from fcc to bcc stacking. The detailed identification of the Burgers vector of the $[\bar{1}01]_{fcc}$ screw dislocations is provided in Appendix E.

Second, there are screw dislocations with kinks, having $a_{bcc}/2\,[1\bar{1}1]$ Burgers vector and gliding on the $(\bar{1}01)_{bcc}$ in the bcc phase with a line direction in the interface, as seen in Figure 5c and sketched in Figure 5b (see Appendix H). These dislocations arise naturally to accommodate the tilt angle $\varphi$ on the $(111)_{fcc} \parallel (011)_{bcc}$ plane. These screw dislocations reside on the bcc side of the terrace plane, and have edge-character kinks in $(\bar{1}01)_{bcc}$ out of the terrace plane, which are readily identified with a Burgers circuit construction in bcc (Fig. 6a). This is consistent with the measured Burgers vector and the $\sim [0\bar{5}7]_{fcc}$ lines of contrast identified with TEM[9] in laths with $\sim (575)_{fcc}$ habit plane. This defect was often speculated to be a screw dislocation in fcc[4,8,9]. The spacing of the $a_{bcc}/2\,[1\bar{1}1]$ defects is ~2.55 nm, close to measurements[9] (2.6 - 6 nm).

The interfaces for all orientations ($\varphi = 3.11°, 4.75°, 5.21°, 5.7°$) in/near the experimental range have the same defect structure, as shown in Figure 7. The orientation determines only the habit plane, the average step spacing, and the spacing and line direction of the bcc dislocations; the step direction and associated screw dislocation are fixed by the imposed boundary conditions. The atomistic simulations thus provide a unified picture of the interface similar to that of the TM model: there are two sets of defects whose spacing and/or line direction varies to accommodate the orientation.

Figure 8 shows the structures obtained for the KS orientation ($\varphi = 0°$) and an orientation outside of the experimental range ($\varphi = 10°$). For the KS orientation, there are no bcc dislocations (their spacing is infinite). The screw dislocation along the step is now compact with slip plane and direction identical to a bcc screw (see Appendix E). There are also multiple step heights, which differs from the DFT simulation (Figure 3) because the atomistic simulation is performed on a much larger unit cell that enables the interface to adopt a lower-energy structure with multiple step heights; this will later be predicted by the theory. At $\varphi = 10°$, well above the experimental range, the interface has an entirely different and complex structure. We discuss these interfaces further below when we address interface motion.

We now discuss the possible influence of simulation constraints and interface construction methods on the observed interface structure. The interface structures here satisfy periodic boundary conditions. In particular, the step orientation $[\bar{1}01]_{\mathrm{fcc}}$ is taken as a periodic direction according to direct HRTEM observations[4,13] in Fe-Ni-Mn. Deviations of the step line from $[\bar{1}01]_{\mathrm{fcc}}$ are possible in real materials, and are predicted by theory (see below and TM), in which case the $[\bar{1}01]_{\mathrm{fcc}}$ screw dislocations would become kinked. We discuss implications of this on interface motion below. The parallelism between $(111)_{\mathrm{fcc}}$ and $(011)_{\mathrm{bcc}}$ at the interface is not enforced, but is the

result of atomic relaxations: tilts of few degrees can be present between the two phases far from the interface, but the system tries in all cases to achieve parallel close-packed planes at the interface. This is consistent with TEM observations[10], showing parallelism of these planes at the interface even when a few degrees of mismatch exists far from the interface[39]. Finally, Figure 4a shows one apparent extra $(1\bar{1}1)_{\mathrm{fcc}}$ plane along the periodic direction $[\bar{3}4\bar{3}]_{\mathrm{fcc}}$; this is not an extra plane in fcc but is due to the presence of the $a_{\mathrm{bcc}}/2\,[1\bar{1}1]$ edge dislocation core in the bcc-like plane just above. Such "extra planes" are sometimes observed in HRTEM, and might disappear for a specific lattice parameter ratio (1.247) and habit plane orientation $(121)_{\mathrm{fcc}}$ (e.g., Fe-Ni-Mn alloys considered in Refs. 4, 13) because in such specific cases there is perfect matching of atomic distances in bcc and fcc along the $[\bar{1}1\bar{1}]_{\mathrm{fcc}}$ direction.

Overall, the interface structure found atomistically is fully consistent with multiple TEM experiments[4,9], and provides a clear and physical identification of the precise nature of the interfacial defects. This is the first main result of this paper.

## 4. Interface motion: origins of glissile/athermal motion

The atomistic fcc-bcc interfaces for orientations $\varphi = 3.11°, 4.75°, 5.21°, 5.7°$, within or very near the experimental range, are all glissile/athermal, i.e. at T=0K these interfaces glide at zero applied shear stress. The interface in Fig. 4 is actually pinned by undetectable structural features, and minute adjustments lead to an interface that glides at T=0K and zero stress (Appendix F). The interface in Fig. 4 glides at T=0K under the application of a small shear strain corresponding to just 1 MPa shear stress in the direction of the transformation. A movie of the $\varphi = 4.75°$ gliding interface is shown in Supplementary Online material.

Athermal motion at T=0K could be caused by a very strong thermodynamic driving force for the fcc to bcc transition. For this MEAM potential, the Gibbs free energy

difference between fcc and bcc is ~8.5 meV/atom at T=0K. We have thus studied the behavior of the interface at finite temperatures up to 600K. At 600K, the Gibbs free energy difference is reduced down to ~3.0 meV/atom, and so is much smaller. Nonetheless, at all temperatures, the interface structures for $\varphi = 3.11°, 4.75°, 5.21°, 5.7°$ are maintained and the interfaces remain glissile/athermal (athermal at finite-T meaning that it moves very rapidly with no evidence of thermal activation that would reduce the net velocity). Thus, the glissile/athermal motion is not artificially driven by a large driving force (see Appendix G for further details).

Experimentally, "isothermal" martensite can be observed, i.e. situations arise where the macroscopic interface motion appears thermally-activated. However, it is well-established[13,15,16] that this behavior is not related to the intrinsic structure and motion of the interface, which needs to be glissile to avoid local atomic diffusion[16]. This has been demonstrated by multiple studies, as reported by Christian[15] and concluded by Ogawa and Kajiwara[13], showing that the interface of steel grades where "isothermal" martensite forms has the same features as those of Fe-Ni-Co-Ti and Fe-Cr-C alloys where athermal martensite forms. The isothermal (thermally-activated or rate-dependent) martensite formation is thus understood to be an extrinsic phenomenon, due to the interaction of the interface with dislocations in the austenite matrix (perhaps generated by plastic flow caused by stresses created by the transformation strain itself).

Analyzing the detailed atomic motions for $\varphi = 4.75°$, Figures 9a,b show the upper interface of the bicrystal before and after applying a shear displacement of $\mathrm{b} = \mathrm{a_{fcc}}/2[\bar{1}01]$ at the top surface. Only the interface moves to accommodate the applied displacement, and the defects are observed to glide with the interface (see movies in Supplementary Online material). There is no change in local crystalline configuration nor creation/elimination of sites or defects. Figure 9c shows the detailed atomic

displacements at the interface for load along the $[\bar{1}01]_{fcc}$ direction. There is a displacement difference of ~b between bcc and fcc along the phase transformation direction, with out-of-plane displacements negligible. In the interface region, the two main contributions to the atomic displacements are the relative gliding of the atoms along $[\bar{1}01]_{fcc}$ (glide of the screw dislocations) and the relative sliding of atoms along $[1\bar{1}1]_{bcc}$ (glide of the bcc kinks), see Appendix H. The bcc dislocations glide on the $(\bar{1}01)_{bcc}$ plane in the bcc phase (see Appendix H). The atomic displacements become homogeneous outside of the interface region and align approximately parallel to the interface, along the $[\bar{1}01]_{fcc}$ + 19.5° direction. Measuring the distance swept by the interface defects on the $(111)_{fcc}$ plane, we estimate a transformation strain of 59%.

These interfaces are athermal because the edge-character kinks belonging to the screw dislocations in the bcc phase move at very low stress, and can push the fcc screw dislocations, which in turn glide almost spontaneously into the fcc phase. Discussion of our results relative to the literature regarding necessary conditions for a glissile interface is provided in Appendix I.

The interfaces with $\varphi = 0°$, 10° (KS and outside the experimental range) are not glissile/athermal. The $\varphi = 0°$ interface (KS orientation) with no bcc screw dislocations requires ~440 MPa stress to move at T=0K. The remaining fcc screw dislocation along the step now actually has collapsed to effectively a bcc screw dislocation, which has high Peierls stress (see Appendix E). Theory (see below) predicts that the actual KS interface has a step direction at an angle from $[\bar{1}01]_{fcc}$, which requires the formation of kinks of edge character. These kinks should be able to move athermally. The complex $\varphi = 10°$ interface requires 1100 MPa at T=0K to move because the glissile interface structure has disintegrated (Fig. 8b). All the bcc dislocations, which would be very closely spaced, have crossed the interface into the fcc phase and this completely eliminates the ability of the interface to move. The kinks of the bcc screw dislocations are able to cross into fcc

because the $[1\bar{1}1]_{\mathrm{bcc}}$ direction becomes very close to $[0\bar{1}1]_{\mathrm{fcc}}$, and hence the barrier for slip transmission from one phase to the other is low. Furthermore, there are no screw dislocations, only mixed dislocations (indicated with Burgers vector $\mathbf{b}_2$ in Figure 8b) that accommodate the misfit along the $[\bar{1}01]_{\mathrm{fcc}}$ direction. This is consistent with theory (see Section 5 below), which predicts that an interface with the "glissile/athermal" structure found for the observed orientation range is not possible for this orientation angle. There is thus no feasible arrangement of screw dislocations that is capable of accommodating the misfit along $[\bar{1}01]_{\mathrm{fcc}}$, and hence mixed dislocations are the only possible solution.

Our results rationalize the origins of the glissile/athermal interface in the experimentally-observed range of φ. The results also imply why the experimental range is observed – it corresponds to the range over which the interface defects are such that the interfaces are indeed glissile/athermal, enabling the fastest rate of transformation to the low-energy bcc phase. The glissile and athermal nature, and mechanism of motion, of the interface is the second main result of this paper.

## 5. New theory of the fcc/bcc transformation

We now incorporate the observed defect structures into a new crystallographic theory for the martensitic transformation. The theory predicts the habit plane normal vector $\boldsymbol{n}^{(1)}$, shear transformation direction $\boldsymbol{s}^{(1)}$, and magnitude $m^{(1)}$ of the shear transformation strain, as the elements of the overall compatible shape deformation tensor of the form $\boldsymbol{P}^{(1)} = \boldsymbol{I} + m^{(1)}\boldsymbol{s}^{(1)} \otimes \boldsymbol{n}^{(1)}$ where $\boldsymbol{I}$ is the identity tensor, which must have the form of a pure shear deformation. The historical PTMC theories have been labeled as "phenomenological" because the choice of defects has been made with some combination of (i) experimental input, (ii) assumptions of what might exist, and/or (iii) broad searching across a range of defects without direct connection to the interface structure. The Topological Model was applied specifically to use

crystallography to identify possible defects, but has to date been executed only within a constrained set of defects required to lie in the terrace plane and is generally unable to assess additional atomic-scale accommodations. Here, our choice of defects is determined by the atomistic simulations, which automatically satisfy all crystallographic considerations as well as additional features beyond crystallography, and hence we label this theory as a "predictive" theory for martensitic crystallography.

The theory starts with the well-known homogeneous fcc to bcc lattice transformation[15-19,25-27] $\boldsymbol{S} = \boldsymbol{R} \cdot \boldsymbol{B}$ where $\boldsymbol{B}$ is the Bain strain tensor (actually the deformation gradient tensor)

$$\boldsymbol{B} = \begin{bmatrix} \sqrt{2}\frac{a_{bcc}}{a_{fcc}} & 0 & 0 \\ 0 & \sqrt{2}\frac{a_{bcc}}{a_{fcc}} & 0 \\ 0 & 0 & \frac{a_{bcc}}{a_{fcc}} \end{bmatrix}$$

and $\boldsymbol{R} = \boldsymbol{R}_{\varphi} \cdot \boldsymbol{R}_{\psi}$ is a composite rotation tensor defining the orientation relationship at the interface (see Figure 2); both are uniquely determined by $a_{fcc}/a_{bcc}$ and the orientation $\varphi$. The Bain correspondence is adopted here (see Fig. 2). No "shuffling" is needed to achieve the correct orientation[15], because the Bain strain yields the correct change in atomic stacking from fcc to bcc. Since this bcc phase is now misoriented and misfitting with respect to the original fcc phase, there must be additional shear deformations of the bcc phase "at" the interface that bring the bcc crystal into (average) registry with the fcc crystal along some fcc crystalline plane (the habit plane) defined by the shear deformation $\boldsymbol{P}^{(1)}$. The observed $\boldsymbol{P}^{(1)}$ is thus related to $\boldsymbol{S}$ via two other lattice-invariant shear deformations $\boldsymbol{P}^{(2)}$ and $\boldsymbol{P}^{(3)}$ of the bcc crystal as

$$\boldsymbol{P}^{(1)} = \boldsymbol{R}_{\Delta} \cdot \boldsymbol{S} \cdot \boldsymbol{P}^{(3)} \cdot \boldsymbol{P}^{(2)}$$

where $\boldsymbol{P}^{(i)} = \boldsymbol{I} + m^{(i)}\boldsymbol{s}^{(i)} \otimes \boldsymbol{n}^{(i)}$. The shears $\boldsymbol{P}^{(2)}$ and $\boldsymbol{P}^{(3)}$ are associated with two sets of interface defects as described below.

The rotation $\boldsymbol{R}_{\Delta}$ is introduced as a new, small, but essential, corrective rotation that

connects the far-field ($\boldsymbol{R}'$) and interface ($\boldsymbol{R}$) orientations, $\boldsymbol{R}' = \boldsymbol{R}_\Delta \cdot \boldsymbol{R}$, which differ slightly in experiments[38] and also in our simulations. For instance, some of the bcc atomic planes in Figure 1b are clearly curved, and this is seen more clearly in Appendix A as deviations of assumed straight planes of atoms. $\boldsymbol{R}_\Delta$ is usually neglected[19], or absent when both defects are assumed to be in the fcc phase[17,18]. While very small, without $\boldsymbol{R}_\Delta$, the theory (as well as the standard PTMC and the TM model) would predict a single unique interface orientation $\varphi$ for a given $a_{fcc}/a_{bcc}$. This would conflict with both experiments and our simulations, which show the possibility of having interfaces with different $\varphi$ for the same lattice parameter ratio. Once $\boldsymbol{B}$ and the shears $\boldsymbol{P}^{(2)}$ and $\boldsymbol{P}^{(3)}$are defined, the shape deformation $\boldsymbol{P}^{(1)}$ can be uniquely computed and then $\boldsymbol{R}_\Delta$ can also be uniquely determined.

Guided by the atomistic structure, we assign $P^{(2)}$ as the shear due to the $a_{bcc}/2[1\bar{1}1]$ screw dislocations gliding on $(\bar{1}01)_{bcc}$; *this choice has never been considered previously*. The shear $m^{(2)}$ is fixed by the orientation $\varphi$ as $m^{(2)} = \frac{2\,\sin\varphi}{\sqrt{3}\sin\zeta\,\sin(\zeta-\varphi)}$, where $\zeta = \cos^{-1}\left(\frac{1}{3}\right) \simeq 70.53°$. We assign $\boldsymbol{P}^{(3)}$ as the shear due to the $a_{fcc}/2[\bar{1}01]$ screws gliding on the $(111)_{fcc}$ plane (Figure 9a); this is the standard assumption[17]. *However*, the magnitude $m^{(3)}$ of this shear must be determined. Each screw dislocation is accompanied by a step, but the step height is not pre-determined. In both experiments and simulations, step heights of multiple integers of the $(111)_{fcc}$ plane spacing $\frac{a_{fcc}}{\sqrt{3}}$ are observed (see Figs. 1 and 4). We introduce the new physical parameter $\beta$ as the *average* step height normalized by $\frac{a_{fcc}}{\sqrt{3}}$, which is equivalent to the *average* screw separation along $(111)_{fcc}$, with the requirement that $\beta \geq 1$. The strain $m^{(3)}$ is the *average* slip on each $(111)_{fcc}$ plane and so $m^{(3)} = \frac{1}{\beta}\sqrt{3/2}$.

A proper theory must thus *predict* a value of $\beta \geq 1$ and be consistent with experimental/simulation observations. Existing HRTEM[4,13] experiments do not

identify the screw dislocations, but show steps of different height. Counting step heights instead of screw dislocations provides a range of $\beta$ because the local atomic details needed to define the steps are not always clear, both in micrographs and in simulations. For example, in the simulations, we can count the stacking faults at $\varphi = 4.75°$ and obtain $\beta = 1.5$ but when we count steps, after careful examination of different cross-sections, we can only determine $1.2 \leq \beta \leq 1.5$; the latter is consistent with a distribution of steps of normalized heights 1 and 2 and contains the exact value $\beta = 1.5$.

The observed shear $\boldsymbol{P}^{(1)}$ is now determined by setting $\boldsymbol{P}^{(1)} = \boldsymbol{R}_\Delta \cdot \boldsymbol{S} \cdot \boldsymbol{P}^{(3)} \cdot \boldsymbol{P}^{(2)}$ and then determining the value of $\beta$ for which $\boldsymbol{P}^{(1)}$ has the form of an invariant shear strain, $\boldsymbol{P}^{(1)} = \boldsymbol{I} + m^{(1)}\boldsymbol{s}^{(1)} \otimes \boldsymbol{n}^{(1)}$. This is achieved when one of the Principal Stretches (eigenvalues) of $\boldsymbol{U} = \sqrt{[\boldsymbol{P}^{(1)}]^T \cdot \boldsymbol{P}^{(1)}}$ equals unity, and the solution is unique. The magnitude, direction, and plane of slip are then determined by the other two eigenvalues ($\lambda_{\max}$, $\lambda_{\min}$), and their eigenvectors ($\boldsymbol{e}_{\max}$,$\boldsymbol{e}_{\min}$), as

Habit plane normal: $$\boldsymbol{n}^{(1)} = \sqrt{\frac{\lambda_{\max}^2 - 1}{\lambda_{\max}^2 - \lambda_{\min}^2}}\,\boldsymbol{e}_{\max} \pm \sqrt{\frac{1 - \lambda_{\min}^2}{\lambda_{\max}^2 - \lambda_{\min}^2}}\,\boldsymbol{e}_{\min}$$

Transformation direction: $$\boldsymbol{s}^{(1)} = \lambda_{\min}\sqrt{\frac{\lambda_{\max}^2 - 1}{\lambda_{\max}^2 - \lambda_{\min}^2}}\,\boldsymbol{e}_{\max} \mp \lambda_{\max}\sqrt{\frac{1 - \lambda_{\min}^2}{\lambda_{\max}^2 - \lambda_{\min}^2}}\,\boldsymbol{e}_{\min}$$

Transformation strain: $$m^{(1)} = \lambda_{\max} - \lambda_{\min}$$

Out of the two possible solution for $\boldsymbol{s}^{(1)}$ and $\boldsymbol{n}^{(1)}$, the one which yields $\boldsymbol{n}^{(1)}$ the closest to the crystallographic habit plane $(111)_{\text{fcc}}$ is considered; this result is independent of $\boldsymbol{R}_\Delta$. Subsequently, $\boldsymbol{R}_\Delta = \boldsymbol{P}^{(1)} \cdot \left(\boldsymbol{S} \cdot \boldsymbol{P}^{(3)} \cdot \boldsymbol{P}^{(2)}\right)^{-1}$ is computed. The step line direction $\boldsymbol{s}$ is also computed as $\boldsymbol{s} = \boldsymbol{n}^{(3)} \times \boldsymbol{n}^{(1)}$, and the angle $\xi = \cos^{-1}\left(\boldsymbol{t}^{(3)} \cdot \boldsymbol{s}\right)$ indicates its deviation from the screw line $\boldsymbol{t}^{(3)}$ on the $(111)_{\text{fcc}}$ plane. Using the defects found in the simulations, the only inputs to the theory are the ratio $a_{fcc}/a_{bcc}$ between fcc and bcc lattice parameters and the angle $\varphi$ characterizing the local orientation relationship.

Table 1 shows the validation of the crystallographic theory with respect to the simulations for both $\varphi = 4.75°$ and $\varphi = 3.11°$. We use the lattice parameter ratio measured in the simulations far from the interface because the (average) elastic misfit-free interface is only achieved for the exact irrational habit plane predicted by the theory and the finite simulations slightly deviate from theory and accommodate these deviations elastically. The predictions of the crystallographic theory for $\varphi = 4.75°$ are in excellent agreement with the simulation results in all respects, especially including the average step height $\beta$. The predicted $\boldsymbol{R}_\Delta$ corresponds to orientation differences $d\theta$ between $(111)_{\text{fcc}}$ and $(011)_{\text{bcc}}$ around $[\bar{1}01]_{\text{fcc}}$, $d\chi$ around $[\bar{1}2\bar{1}]_{\text{fcc}}$, and $d\varphi$ around $[111]_{\text{fcc}}$. The predicted $d\theta$ is consistent with simulations, while constraints in the simulations prevent $d\varphi \neq 0°$ and $d\chi \neq 0°$. The step line direction, indicated by the angle $\xi$ with respect to $[\bar{1}01]_{\text{fcc}}$ on the $(111)_{\text{fcc}}$ plane, is nearly zero, while constrained to be $\xi = 0°$ in simulations.

The theory predictions for $\varphi = 3.11°$ are also in good agreement with simulation results in nearly all respects. The main difference relates to the step direction, which is again enforced to $\xi = 0°$ in the simulations while theory predictions yield $\xi = 3.5°$.

The predicted step line direction is not exactly along $[\bar{1}01]_{\text{fcc}}$. The predicted geometry can be realized as consisting of segments of steps and screws along $[\bar{1}01]_{\text{fcc}}$ with kinks spaced by $s_\xi = \frac{b}{\tan\xi}$. If $s_\xi \gg b$ then a feasible arrangement of isolated fcc kinks is possible. Due to both size and complexity, it is not possible to construct simulations cells that would enable study of any such kinked structures. But note that the crystallographic theory is not affected by having (or not) fcc kinks, since the input $\boldsymbol{P}^{(3)}$ carries no information about the character of the fcc dislocation, and thus the theory is independent of the exact dislocation character. For $\varphi = 4.75°$, the kink spacing is quite large. For $\varphi = 3.11°$, the kink spacing is $\sim 4$ nm, which is reflected by the deviation of the predicted habit plane from $(\text{xyx})_{\text{fcc}}$. The theory also predicts a

line direction of $\sim 4.5°$ from $[\bar{1}01]_{\mathrm{fcc}}$ for the KS orientation ($\varphi = 0°$) and thus slightly smaller kink spacing. However, the predicted presence of such kinks would provide a mechanism for glide of the KS interface wherein the kinks glide on $(111)_{\mathrm{fcc}} \parallel (011)_{\mathrm{bcc}}$ to carry the interface motion athermally.

Extending the theory to higher misorientation angles, the theory predicts $\beta \leq 1$ for $\varphi \geq 7°$. This implies that such interfaces cannot exist while maintaining the interface structure defined by the two defects found in simulations. Thus, some different interface structures must form. This accounts for the breakdown of the interface into a new structure that is observed in simulations for $\varphi = 10°$ (Figure 8b).

| | Simulations | Theory | Simulations | Theory |
|---|---|---|---|---|
| $\frac{a_{\mathrm{fcc}}}{a_{\mathrm{bcc}}}$ | $\simeq 1.2537$ | 1.2537 | $\simeq 1.2518$ | 1.2518 |
| $\varphi$ | 4.75° | 4.75° | 3.11° | 3.11° |
| $\beta$ | 1.5 | 1.515 | 1.46 | 1.552 |
| $\boldsymbol{n}^{(1)}$ | $(2\ 3\ 2)_{\mathrm{fcc}}$ | $(2\ 3\ 2)_{\mathrm{fcc}}$ | $(10\ 17\ 10)_{\mathrm{fcc}}$ | $(10.5\ 17.6\ 10)_{\mathrm{fcc}}$ |
| $\boldsymbol{s}^{(1)}$ | $[\bar{1}\ 0\ 1]_{\mathrm{fcc}} + 19.5°$ | $[\bar{1}\ 0\ 1]_{\mathrm{fcc}} + 19.5°$ | $[\bar{1}\ 0\ 1]_{\mathrm{fcc}} + 19.9°$ | $[\bar{1}\ 0\ 1]_{\mathrm{fcc}} + 20.4°$ |
| $m^{(1)}$ | 0.59 | 0.57 | 0.55 | 0.56 |
| $d\theta$ | 0.34° | 0.28° | 0.49° | 0.34° |
| $d\varphi$ | 0° (constrained) | $-0.15°$ | 0° (constrained) | 0.017° |
| $d\chi$ | 0° (constrained) | $-0.003°$ | 0° (constrained) | 0.021° |
| $\xi$ | 0° (constrained) | 0.38° | 0° (constrained) | 3.5° |
| $s_\xi$ | ---- | 37.9 nm | ---- | 4.1 nm |

**Table 1 | Predictions of the theory for martensitic transformations versus simulations.** Predictions use the ratio between the bulk bcc and fcc lattice parameter measured in simulations far from the interface. The theory matches all aspects of the simulation well.

The success of the new theory here in predicting many features of the simulations, within constraints of the simulations, including multiple step heights and a range of orientations for a fixed lattice parameter ratio, is the third main result of this paper, and now motivates applications of the theory to real Fe-based steels.

## 6. Application of the theory to Fe-Ni-Mn and Fe-C

Table 2 shows predictions of the crystallographic theory for Fe-Ni-Mn alloys along with experimental results. For Fe-Ni-Mn, we use the measured *average* orientation $\bar{\varphi}$ and measured alloy lattice constants; there are no adjustable parameters. The predicted details of the transformation are within the experimental range for all quantities, and the predicted $\beta = 1.69$ is consistent with a distribution of steps of heights $\geq 1$, as observed (Fig 1). The transformation strain is larger, but not significantly larger, than the lower bound experimental result. The predicted $(d\theta, d\chi, d\varphi)$ are small, consistent with one experiment where they were studied[38]. The deviation of the step line from $[\bar{1}01]_{\text{fcc}}$ is very small, consistent with HRTEM observations of step line parallel to $[\bar{1}01]_{\text{fcc}}$ [4,13], and the predicted average fcc kink spacing is large, and much bigger than typical HRTEM specimen thickness.

Table 3 shows predictions of the crystallographic theory for Fe-C alloys along with experimental results. For Fe-C, we consider the average measured $\bar{\varphi}$ as well as values at the measured +/-1° standard deviation[10] so as to elucidate trends with orientation. We also consider the experimental range of alloy lattice constants associated with varying austenite C content in low C steels[39]. For all $\varphi$, we predict a habit plane consistent with experiments and predict $1.01 \leq \beta \leq 1.61$ again in the physical range and consistent with a distribution of observed step heights between 1 and 2 units.

| | Experiments<br>Fe-20Ni-5Mn[§]<br>Refs. 4,8,13,14 | Theory |
|---|---|---|
| $\frac{a_{\mathrm{fcc}}}{a_{\mathrm{bcc}}}$ | $\simeq 1.247$<br>$\bar{\varphi} \simeq 3.8°$ | $1.247$<br>$\varphi = 3.8°$ |
| $\beta$ | $\sim 1.2 - 2.3$* | 1.69 |
| $\boldsymbol{n}^{(1)}$[§§] | 9.5° to 19.5° | 15.6° |
| $\boldsymbol{s}^{(1)}$ | ---- | $[\bar{1}01]_{\mathrm{fcc}} + 22.4°$ |
| $m^{(1)}$ | $> 0.3$ [14] | 0.50 |
| $d\theta$ | ---- | 0.28° |
| $d\varphi$ | ---- | $-0.15°$ |
| $d\chi$ | ---- | 0.00° |
| $\xi$ | $\sim 0°$ [4,13] | 0.18° |
| $s_\xi$ | ---- | 79.8 nm |

[§] The lattice parameter of bulk bcc ($a_{\mathrm{bcc}} = 2.87$ Å) and fcc ($a_{\mathrm{fcc}} = 3.58$ Å) are from XRD measurements on a Fe-23Ni-3.8Mn alloy[13], since Refs. 4, 8 and 14 do not provide lattice parameters.

* $\beta$ parameters are estimated from two HRTEM micrographs[4,13], see Fig. 1.

[§§] Habit planes are stated in terms of the misorientation $\theta$ with respect to $(111)_{\mathrm{fcc}}$ ($\theta = 0°$) around the step line direction ($[\bar{1}01]_{\mathrm{fcc}}$ axis in experiments). Typical orientations observed in experiments are $(575)_{\mathrm{fcc}}$ ($\theta = 9.5°$), $(232)_{\mathrm{fcc}}$ ($\theta = 11.4°$), $(353)_{\mathrm{fcc}}$ ($\theta = 14.4°$) and $(121)_{\mathrm{fcc}}$ ($\theta = 19.5°$).

**Table 2 | Predictions of the theory versus experiments on Fe-Ni-Mn alloys.**

Predictions are made using the average orientation $\bar{\varphi}$ and measured lattice constants. The habit plane range is based on TEM analyses[8] and HRTEM[4,13] micrographs.

| $\frac{a_{\mathrm{fcc}}}{a_{\mathrm{bcc}}}$ | Experiments Fe-C alloys* Refs. 10,12,39-42 | Theory | | | | | |
|---|---|---|---|---|---|---|---|
| | $1.25-1.274$ | $1.25$ | | | $1.274$ | | |
| | $\bar{\varphi}=2.5°\pm1°$ | $\varphi=1.5°$ | $\varphi=2.5°$ | $\varphi=3.5°$ | $\varphi=1.5°$ | $\varphi=2.5°$ | $\varphi=3.5°$ |
| $\beta$ | ---- | 1.51 | 1.56 | 1.61 | 1.1 | 1.08 | 1.01 |
| $\boldsymbol{n}^{(1)\S}$ | 9.5° to 14.4° | 17.6° | 16.5° | 15.1° | 11.9° | 10.3° | 8.34° |
| $\boldsymbol{s}^{(1)}$ | ---- | $[\bar{1}01]_{\mathrm{fcc}}$ +19.9° | $[\bar{1}01]_{\mathrm{fcc}}$ +20.7° | $[\bar{1}01]_{\mathrm{fcc}}$ +21.2° | $[\bar{1}01]_{\mathrm{fcc}}$ +13.7° | $[\bar{1}01]_{\mathrm{fcc}}$ +13.6° | $[\bar{1}01]_{\mathrm{fcc}}$ +13.0° |
| $m^{(1)}$ | ---- | 0.59 | 0.56 | 0.53 | 0.85 | 0.87 | 0.94 |
| $d\theta$ | $<2.0°$ | 0.37° | 0.34° | 0.317° | 0.46° | 0.39° | 0.32° |
| $d\varphi$ | ---- | 0.21° | 0.07° | −0.06° | 0.37° | 0.25° | 0.15° |
| $d\chi$ | ---- | 0.03° | 0.02° | 0.01° | 0.10° | 0.08° | 0.06° |
| $\xi$ | ---- | 5.14° | 3.99° | 2.06° | 11.4° | 11.1° | 10.2° |
| $s_\xi$ | ---- | 2.8 nm | 3.59 nm | 6.95 nm | 1.24 nm | 1.27 nm | 1.39 nm |

* The room temperature bulk bcc lattice parameters at either 0 GPa ($a_{\mathrm{bcc}}=2.865$ Å) or 3 GPa ($a_{\mathrm{bcc}}=2.848$ Å) are used[41]. C below 0.6wt% in martensite leads to negligible tetragonal distortions and can slightly increase (<1%) the bcc lattice parameter[43]. C saturated bcc lattice parameters are also considered according to Ref. 43. The fcc austenite lattice parameters are taken in the range $3.59\ \text{Å} \le a_{\mathrm{fcc}} \le 3.63\ \text{Å}$, according to XRD measurements on low carbon steels (Fig. 4a in Ref. 39).

§ Habit planes are stated in terms of the misorientation $\theta$ with respect to $(111)_{\mathrm{fcc}}$ ($\theta=0°$) around the step line direction ($[\bar{1}01]_{\mathrm{fcc}}$ axis in experiments, which generally neglect possible deviations $\xi$ of the step line direction). Typical orientations observed in experiments are $(575)_{\mathrm{fcc}}$ ($\theta=9.5°$), $(232)_{\mathrm{fcc}}$ ($\theta=11.4°$), $(353)_{\mathrm{fcc}}$ ($\theta=14.4°$) and $(121)_{\mathrm{fcc}}$ ($\theta=19.5°$).

**Table 3 | Predictions of the theory versus experiments on Fe-C alloys.** Predictions are made for a range of orientations $\bar{\varphi}$ spanning the reported values, and for lattice parameters corresponding to the expected range of C content in the austenite phase. Habit planes refers to multiple TEM analyses[10,42].

The results for Fe-C show that all the main features related to the shape deformation (transformation strain, habit plane and transformation direction) depend on the fcc/bcc lattice parameter ratio, which is alloy specific, while but are weakly dependent on the specific orientation relationship $\varphi$, which can vary experimentally from KS to NW within the same alloy[12,18]. In general, trends show that the higher the lattice parameter ratio, the bigger the transformation strain $m^{(1)}$ and the lower the angle $\theta$ between habit plane and $(111)_{\mathrm{fcc}}$ plane. The trends in the average step height $\beta$ change as a function of the $a_{fcc}/a_{bcc}$ ratio. At low ratios (1.25), $\beta$ decreases with decreasing $\varphi$, while at higher ratios (1.274), $\beta$ decreases with increasing $\varphi$. Finally, as the lattice parameter ratio increases, the deviation of the step line from pure screw orientation increases significantly. For the experimental Fe-C lattice parameter ratios, the predicted fcc kink spacing is still consistent with an atomistic picture of straight screw segments and edge-character kinks. We discuss more outcomes below.

The success of the new theory in predicting experiments is completely independent of the atomistic simulations, and in particular of the chosen interatomic potential. The theory only uses the defects identified in the simulations, and these defects could have been postulated a priori. The new theory also introduces both $\beta$ and $\boldsymbol{R}_{\Delta}$ that make essential contact with experimental observations. The success of the new theory is the fourth main result of this paper.

## 7. Implications of the theory for design of alloys

Our new understanding of the fcc-bcc interface defects now provides a quantitative framework for material and microstructure design across the scope of multiphase steels, including bainitic steels (see Appendix J) and other materials relying on martensitic transformations[21].

Of particular importance is the prediction of the transformation strain $m^{(1)}$, which

is crucial to toughening in TRIP steels. Existing continuum models of TRIP steels[44-47] are now widely used for predicting the effective stress-strain behavior of polycrystalline steels[48]. A key input to these all theories is the shear strain $\boldsymbol{P}^{(1)}$ due to transformation of retained austenite. Unlike previous models[18,19], the present theory provides a unique and physically-based value for this quantity as a function of the underlying material.

Specifically, with the defects now firmly established, the theory predicts $m^{(1)}$ to depend only on $a_{fcc}/a_{bcc}$ and the orientation $\varphi$. Moreover, $m^{(1)}$ (as well as $\boldsymbol{s}^{(1)}$ and $\boldsymbol{n}^{(1)}$) is mainly controlled by $a_{fcc}/a_{bcc}$; $\varphi$ is much less important (See Fe-C systems in Table 3). The transformation strain can vary strongly with $a_{fcc}/a_{bcc}$, ranging from ~0.55 to ~0.95 across the Fe-C alloys. For design, changes in $a_{fcc}/a_{bcc}$ can be predicted by first-principles methods and then the theory can be used to predict $m^{(1)}$. A computational search can then be performed to find materials that maximize $m^{(1)}$. While the development of new materials requires consideration of many factors, the ability to include accurate predictions of the maximum transformation strain provides an important input, especially for designing materials for high ductility.

The theory also provides a means of determining the limits over which the fcc-bcc interface defects, required for glissile/athermal motion, can occur. For a given $\varphi$, the theory predicts that there is a maximum lattice parameter ratio above which $\beta < 1$, which is unphysical. The theory thus suggests that larger values of the lattice parameter ratio cannot have the glissile/athermal structure found here. For the Fe-C system at $\varphi = 3.5°$, for instance, the theory predicts that $\beta < 1$ for $a_{fcc}/a_{bcc} > 1.274$. In fact, $a_{fcc}/a_{bcc}>1.274$ corresponds[39] to alloys where C partitioning in the austenite reaches local levels above ~1.3 wt%, comparable to the level (~1.0 wt% C) at which, indeed, there is a clear change in structure found experimentally in the martensite, towards the fcc austenite-bct twinned martensite interface. For lower $\varphi$, the admissible lattice parameter ratio increases, and thus interfaces with higher carbon levels in the austenite

are admissible. This is consistent with the observation[4] of an average $\varphi = 1°$ for carbide-free Fe-C bainite, for which the maximum predicted permissible lattice parameter ratio is $a_{fcc}/a_{bcc}$ = 1.28, which corresponds[49] to C concentrations above 1.5 wt%. The existence of a maximum admissible lattice parameter ratio can also explain why, in bainite formed at 723K, the maximum observed C concentration is 1.61 wt% C [50], well below the paraequilibrium value at this temperature (3.29 wt%). It can also provide insight into the different transformation stages observed in Fe-C bainite[50,51]. It is observed that after the peak concentration of 1.61 wt% C is reached in the retained austenite between the ferritic laths, the transformation stops until carbides form in the austenite. This decreases the austenite C content and can thus allow for formation of new ferrite variants at $a_{fcc}/a_{bcc}$ ratios where this glissile/athermal fcc-bcc interface is admissible. The theory can thus provide limiting material properties for achieving the glissile interface as a function of composition and processing.

The theory may provide the basic insights to enable investigation of other behavior. For instance, the high transformation strain due to the austenite-martensite interface migration may contribute to the "greasy" plane effect[52,53] in the widely-used low carbon lath martensite[40], where localized slip/plasticity occurs[54,55] in the very thin retained austenite films at lath boundaries[56]. Also, the mechanism of mitigation of hydrogen embrittlement[57] by the introduction of thin austenite films within martensite will undoubtedly be influenced by the fact that edge-character kink segments reside in the low-H-solubility martensite phase rather than screw dislocations in the austenite phase. Similarly, knowledge of the interface structure may help identify physical mechanisms for the interaction of alloying solutes (Mn, C, Ni, Si, etc.) with the interface defects, which influences physical properties.

## 8. Comparison with existing PTMC and TM models

As mentioned in the introduction, there is a long history of crystallographic modeling of the fcc-bcc interface in iron alloys. Our work presents many similarities with previous work and confirms many previous assumptions. In contrast with all previous theories, we identify the relevance of the fcc-bcc lattice parameter ratio for determining the transformation strain, and provide a predictive model rather than a range of solutions for a specific material. Compared with PTMC, our theory nails down the possible sets of interface dislocations accommodating the lattice invariant deformation to a single set. Compared with the TM, the model allows for combinations of steps with multiple step heights within the same interface, which provides the flexibility needed to predict experimentally-consistent defect structures for the whole range (KS to NW) of experimentally observed orientation relationships. A detailed comparison is further provided below.

Existing PTMC theories[4,17-19] select two sets of intrinsic defects that relieve the misfit/coherency strains associated with the transformation. These defects are usually[4,17-19] (i) screw dislocations having $a_{fcc}/2[\bar{1}01]$ Burgers vector next to steps aligned with $[\bar{1}01]_{fcc}$; and (ii) screw dislocations with $a_{fcc}/2[0\bar{1}1]$ Burgers vector. The glide planes are either assumed[17] to be $(111)_{fcc}$ and $(100)_{fcc}$ (not an active fcc glide plane) respectively, or not uniquely identified[18,19]. These assumptions predict a habit plane in good agreement with experiments[17-19], but the transformation strain is much too large[17] (~0.96) or falls within such a wide range of values for the same material[18,19] that it provides no useful answer. Furthermore, no PTMC theory predicts explicitly multiple-height steps at the interface (parameter $\beta \geq 1$), nor a mismatch between interface and far-field orientation relationship (corrective rotation $\boldsymbol{R}_{\Delta}$). Unlike existing PTMC theories, in the present work we demonstrate explicitly that the chosen defect combination is glissile and athermal, and provide a detailed picture of the model

(Fig. 5b) which is consistent with experiments and simulations.

A study[20] based on the topological model identified possible interface defect structures, and the outcome shows, in general, subtle differences with respect to our work. First, the $a_{bcc}/2[1\bar{1}1]$ screw dislocations considered here were assigned an arbitrary line direction contained in the $(111)_{fcc}$ plane, while here the line direction is out of that plane and is at the intersection between $(111)_{fcc} \parallel (011)_{bcc}$ and $(\bar{1}01)_{bcc}$ (see Fig. 5b). Second, the combination of $a_{bcc}/2[1\bar{1}1]$ screw dislocations with screw dislocations having $a_{fcc}/2[\bar{1}01]$ is ruled out in TM, while steps with different Burgers vectors and generally different line directions are considered. This TM model also predicts that, in the KS limit, two sets of defects must still exist, while our work (consistent with DFT[34]) shows that only $a_{fcc}/2[\bar{1}01]$ screws are necessary, although probably with kinks to ensure athermal motion. Ref. 20 also does not specify the glide planes of the interface defects nor determine any transformation strain. In contrast, the defects found here in the atomistic interface ($a_{fcc}/2[\bar{1}01]$ screw and $a_{bcc}/2\,[1\bar{1}1]$ screw gliding on $(\bar{1}01)_{bcc}$) lead to excellent predictions of all measured and/or simulated quantities for the fcc-bcc interface. Finally, the defect structure predicted by TM[20] shows some qualitative agreement with experiments only for one specific orientation ($\varphi = 2.76°$), while in our work the predicted defect structure is consistent with experiments all the way from KS to NW.

With respect to TM, we allow multiple step heights in the same system, i.e. $\beta \geq 1$, enabling the flexibility that allows us to find a solution that agrees much better with experiments. Furthermore, the simulations account for actual atomic interactions and configurations, thus include energy in addition to geometry/crystallography. However, the application of TM theory with unit cells multiple step heights (not pursued in Ref. 20) might provide a defect structure close to the revealed in our atomistic simulations. Finally, the TM theory does not envision any far field rotations $\boldsymbol{R}_{\Delta}$, which are observed

in simulations and can be accommodated by defects in the bcc and fcc matrix, as observed experimentally[38]. The TM model developed in Ref. 20 may simply be too constrained in forcing a solution that relaxes the misfit in every individual unit cell of the interface.

## 9. Summary

In summary, a careful atomistic simulation, guided by macroscopic experimental observations and using a validated interatomic potential, reveals the intrinsic defect structure of the fcc/bcc interface in excellent agreement with experiments. The simulation also shows that the interface is glissile and athermal, i.e. moving at T=0K under zero stress. The observed defects are then used to develop a parameter-free predictive crystallographic theory, which is shown to predict all aspects of the simulation and, more importantly, to predict many features of experiments, including multiple step heights, trends with orientation and lattice parameter ratio, and corrective rotations, that are all observed. The parameter-free theory and insights about the defect structure of the interface now provide a foundation for future design and control of this interface, with the potential for enhancing strength and ductility across the wide class of technologically valuable steels where this interface is the key microstructural feature.

## Acknowledgements

F.M. and W.A.C. acknowledge support of this work through a European Research Council Advanced Grant, “Predictive Computational Metallurgy”, ERC grant agreement no. 339081 – PreCoMet.

## References

[1] De Moor, E., Lacroix, S., Clarke, A., Penning, J. & Speer, J.G. Effect of retained austenite stabilized via quench and partitioning on the strain hardening of martensitic steels. *Metall. Mater. Trans. A* **39**, 2586-2595 (2008).

[2] Raabe, D. *et al.* Segregation engineering enables nanoscale martensite to austenite phase transformation at grain boundaries: A pathway to ductile martensite. *Acta Mater.* **61**, 6132-6152 (2013).

[3] Wang, M.-M., Tasan, C.C., Ponge, D., Kotska, A. & Raabe, D. Smaller is less stable: Size effects on twinning vs. transformation of reverted austenite in TRIP-maraging steels. *Acta Mater.* **79**, 268-281 (2014).

[4] Moritani, T., Miyajima, N., Furuhara, T. & Maki, T. Comparison of interphase boundary structure between bainite and martensite in steel. *Scripta Mater.* **47**, 193-199 (2002).

[5] Caballero, F.G. & Bhadeshia, H.K.D.H. Very strong bainite. *Curr. Opin. Solid State Mater. Sci.* **8**, 251-257 (2004).

[6] Nambu, S. *et al.* In situ observations and crystallographic analysis of martensitic transformation in steel. *Acta Mater.* **61**, 4831-4839 (2013).

[7] De Knijf, D., Nguyen-Minh, T., Petrov, R.H., Kestens, L.A.I. & Jonas, J.J. Orientation dependence of the martensite transformation in a quenched and partitioned steel subjected to uniaxial tension. J. Appl. Cryst. **47**, 1261-1266 (2014).

[8] Sandvik, B.P.J. & Wayman, C.M. Characteristics of lath martensite: Part I. crystallographic and substructural features. *Metall. Trans.* A **14**, 809-822 (1983).

[9] Sandvik, B.P.J. & Wayman, C.M. Characteristics of lath martensite: Part II. The martensite-austenite interface. *Metall. Trans.* A **14**, 823-834 (1983).

[10] Kelly, P.M., Jostsons, A. & Blake, R.G. The orientation relationship between lath martensite and austenite in low carbon, low alloy steels. *Acta Metall. Mater.* **38**, 1075-1081 (1990).

693 [11] Miyamoto, G., Takayama, N. & Furuhara, T. Accurate measurement of the orientation
694 relationship of lath martensite and bainite by electron backscatter diffraction analysis. *Scripta*
695 *Mater.* **60**, 1113-1116 (2009).
696 [12] Sandvik, B.P.J. & Wayman, C.M. Crystallography and substructure of lath martensite
697 formed in carbon steels. *Metallography* **16**, 199-227 (1983).
698 [13] Ogawa, K. & Kajiwara, S. High-resolution electron microscopy study of ledge structures
699 and transition lattices at the austenite-martensite interface in Fe-based alloys. *Phil. Mag.* **84**,
700 2919-2947 (2004).
701 [14] Wakasa, K. & Wayman, C.M. The morphology and crystallography of Ferrous lath
702 martensite. Studies of Fe-20%Ni-5%Mn—III. Surface relief, the shape strain and related
703 features. *Acta Metall.* **29**, 1013-1028 (1981).
704 [15] Christian, J.W. *The Theory of Transformations in Metals and Alloys*, 2nd edn (Pergamon
705 Press, Oxford, 1975).
706 [16] Bhadeshia, H.K.D.H. & Wayman, C.M. In: D. Laughlin and K. Hono (Eds.) *Physical*
707 *Metallurgy*, 5th edn, vol I, Ch. 9, 1021-1072 (Elsevier, 2014).
708 [17] Sandvik, B.P.J. & Wayman, C.M. Characteristics of lath martensite: Part III. Some
709 theoretical considerations. *Metall. Trans.* A **14**, 835-844 (1983).
710 [18] Kelly, P.M. Crystallography of lath martensite in steels. *Mater. Trans. JIM* **33**, 235-242
711 (1992).
712 [19] Qi, L., Khachaturyan, J.W. & Morris Jr., J.W. The microstructure of dislocated martensitic
713 steel: Theory. *Acta Mater*. **76**, 23-39 (2014).
714 [20] Ma, X. & Pond, R.C. Parent-martensite interface structure in ferrous systems. *J. Nucl.*
715 *Mater.* **361**, 313-321 (2007).
716 [21] Hirth, J.P. & Pond, R.C. Compatibility and accommodation in displacive phase
717 transformations. *Prog. Mater. Sci.* **56**, 586-636 (2011).
718 [22] Bos, C., Sietsma, J. & Thijsse, B.J. Molecular dynamics simulation of interface dynamics

719 during the fcc-bcc transformation of a martensitic nature. *Phys. Rev. B* **73**, 104117 (2006).

720 [23] Wang, B. & Urbassek, M. Molecular dynamics study of the α–γ phase transition in Fe
721 induced by shear deformation. *Acta Materialia* **61**, 5979-5987 (2013).

722 [24] Ou, X., Sietsma, J. & Santofimia, M.J. Molecular dynamics simulations of the
723 mechanisms controlling the propagation of bcc/fcc semi-coherent interfaces in iron. *Modelling*
724 *Simul. Mater. Sci. Eng.* **24**, 055019 (18pp) (2016).

725 [25] Wechsler, M.S., Lieberman, D.S. & Read, T.A. On the theory of the formation of
726 martensite. *Trans. AIME* **197**, 1503-1515 (1953).

727 [26] Bowles, J.S. & Mackenzie, J.K. The crystallography of martensite transformations I. *Acta*
728 *Metall.* **2**, 129-137 (1954).

729 [27] Khachaturyan, A.G. *Theory of Structural Transformations in Solids* (Dover, New York,
730 2008).

731 [28] Christian, J.W. & Crocker, A.G. In: Nabarro, F.R.N. (Ed.) *Dislocations in Solids*, vol. 3,
732 Ch. 11, 165-252 (North Holland, Amsterdam, 1980).

733 [29] Plimpton, S. J. Fast parallel algorithms for short-range molecular dynamics. *J. Comput.*
734 *Phys.* **117**, 1-19 (1995).

735 [30] Lee, T., Baskes, M.I., Valone, S.M. & Doll, J.D. Atomistic modeling of thermodynamic
736 equilibrium and polymorphism of iron. *J. Phys.: Condens. Matter* **24**, 225404 (2012).

737 [31] Razumovskiy, V.I., Puschnig, P. & Ruban, A.V. Effect of thermal lattice expansion on the
738 stacking fault energies of fcc Fe and $Fe_{75}Mn_{25}$ alloy. *Phys. Rev. B* **93**, 054111 (2016).

739 [32] Lu, S., Ruihuan, L., Kádas, K., Zhang, H., Tian, Y., Kwon, S.K., Kokko, K., Hu, Q.-M.,
740 Hertzman, S. & Vitos, L. Stacking fault energy of C-alloyed steels: The effect of magnetism.
741 *Acta Mater.* **122**, 72-81 (2017).

742 [33] Müller, N., Erhart, P. & Albe, K. Analytic bond-order potential for bcc and fcc iron—
743 comparison with established embedded-atom method potentials. *J. Phys.: Condens. Matter* **19**,
744 326220 (2007).

[34] Jin, H. Atomistic simulations of solute-interface interactions in iron. PhD Thesis, The University of British Columbia (Vancouver), Advisor: Matthias Militzer (2014).

[35] Hirth, J.P. Dislocations, steps and disconnections at interfaces. *J. Phys. Chem. Solids* **55**, 985-989 (1994).

[36] Stukowski, A. Visualization and analysis of atomistic simulation data with OVITO–the Open Visualization Tool. *Model. Simul. Mater. Sci. Eng.* **18**, 015012 (2009).

[37] Stukowski, A. Structure identification methods for atomistic simulations of crystalline materials. *Model. Simul. Mater. Sci. Eng.* **20**, 045021 (2012).

[38] Miyamoto, G., Shibata, A., Maki, T. & Furuhara, T. Precise measurements of strain accommodation in austenite matrix surrounding martensite in ferrous alloys by electron backscatter diffraction analysis. *Acta Mater.* **57**, 1120-1131 (2009).

[39] Jimenez-Melero, E. *et. al.* Martensitic transformation of individual grains in low-alloyed TRIP steels. *Scripta Mater*. **56**, 421-424 (2007).

[40] Morito, S., Huang, X., Furuhara, T., Maki, T. & Hansen, N. The morphology and crystallography of lath martensite in alloy steels. *Acta Mater*. **54**, 5323-5331 (2006).

[41] Zhang, J. & Guyot, F. Thermal equation of state of iron and $Fe_{0.91}Si_{0.09}$. *Phys. Chem. Minerals* **26**, 206-211 (1999).

[42] Luo, C. P. & Liu, J. Crystallography of lath martensite and lower bainite in alloy steels. *Mater. Sci. Eng. A* **438-440**, 149-152 (2006).

[43] Xiao, L., Fan, Z. & Jinxiu, Z. Lattice-parameter variation with carbon content of martensite. I. X-ray-diffraction experimental study. *Phys. Rev. B* **52**, 9970-9978 (1995).

[44] Fischer, F.D., Berveiller, M., Tanaka, K. & Oberaigner, E.R., Continuum mechanical aspects of phase transformations in solids. *Archive App. Mech.* **64**, 54-85 (1994).

[45] Turteltaub, S. & Suiker, A.S.J. Transformation-induced plasticity in ferrous alloys. *J. Mech. Phys. Solids* **53**, 1747-1788 (2005).

[46] Kouznetsova, V.G. & Geers, M.G.D. A multi-scale model of martensitic transformation

771 plasticity. *Mech. Mater.* **40**, 641-657 (2008).

772 [47] Hatami, M.K., Pardoen, T., Lacroix, G., Berke, P., Jacques, P.J. & Massart, T.J. Towards
773 ultra-high ductility TRIP-assisted multiphase steels controlled by strain gradient plasticity
774 effects. *J. Mech. Phys. Solids* **98**, 201-221 (2017).

775 [48] Roters, F., Eisenlohr, P., Hantcherli, L., Tjahjanto, D.D., Bieler, T.R. & Raabe, D.
776 Overview of constitutive laws, kinematics, homogenization and multiscale methods in crystal
777 plasticity finite-element modeling: Theory, experiments, applications. *Acta Mater.* **58**, 1152-
778 1211 (2010).

779 [49] Jimenez-Melero, E., van Dijk, N.H., Zhao, L., Sietsma, J., Offerman, S.E., Wright, J.P. &
780 van der Zwaag, S. Characterization of individual retained austenite grains and their stability in
781 low-alloyed TRIP steels. *Acta Materialia* **55**, 6713-6723 (2007).

782 [50] Tsuzaki, K., Kodai, A. & Maki, T. Formation mechanism of bainitic ferrite in an Fe-2 pct
783 Si-0.6 pct C alloy. *Metallurgical and Materials Transactions A* **25**, 2009-2016 (1994).

784 [51] Yin, J., Hillert, M. & Borgenstam, A. Second stage of upper bainite in a 0.3 mass pct C
785 steel. *Metallurgical and Materials Transactions A* **48**, 1444-1458 (2017).

786 [52] Maresca, F., Kouznetsova, V.G. & Geers, M.G.D. On the role of interlath retained
787 austenite in the deformation of lath martensite. *Modell. Simul. Mater. Sci. Eng.* **22**, 045011
788 (2014).

789 [53] Maresca, F., Kouznetsova, V.G. & Geers, M.G.D. Subgrain lath martensite mechanics: A
790 numerical-experimental analysis. *J. Mech. Phys. Solids* **73**, 69-83 (2014).

791 [54] Mine, Y., Takashima, H., Matsuda, M. & Takashima, K. Micro-tension behaviour of lath
792 martensite structures of carbon steel. *Mater. Sci. Eng.* A **560**, 535-544 (2013).

793 [55] Du, C., Hoefnagels, J.P.M., Vaes, R. & Geers, M.G.D. Plasticity of lath martensite by
794 sliding of substructure boundaries. *Scripta Mater.* **120**, 37-40 (2016).

795 [56] Morito, S., Oh-Ishi, K., Hono, K. & Ohba, T. Carbon enrichment in retained austenite
796 films in low carbon lath martensite steels. *ISIJ Int.* **51**, 1200-1202 (2011).

797 [57] Wang, M.-M., Tasan, C.C., Koyama, M., Ponge, D. & Raabe, D. Enhancing hydrogen
798 embrittlement resistance of lath martensite by introducing nano-films of interlath austenite.
799 *Metall. Mater. Trans.* A **46**, 3797-3802 (2015).
800 [58] Yang, Z. & Johnson, R.A. An EAM simulation of the alpha-gamma iron interface.
801 *Modelling and Simulation in Materials Science and Engineering* **1**, 707-716 (1993).
802 [59] Nagano, T. & Enomoto, M. Calculation of the interfacial energies between α and γ iron
803 and equilibrium particle shape. *Metallurgical and Materials Transactions* A 37, 929-937
804 (2006).
805 [60] Tateyama, S., Shibuta, Y. & Suzuki, T. A molecular dynamics study of the fcc–bcc phase
806 transformation kinetics of iron. *Scripta Materialia* 59, 971-974 (2008).
807 [61] Tateyama, S., Shibuta, Y. & Suzuki, T. Orientation relationship in fcc-bcc phase
808 transformation kinetics of iron: a molecular dynamics study. *ISIJ Int.* **50**, 1211-1216 (2010).
809 [62] Suiker, A.S.J. & Thijsse, B.J. Nucleation, kinetics and morphology of displacive phase
810 transformations in iron. *J. Mech. Phys. Solids* **61**, 2273-2301 (2013).
811 [63] Wang, B. & Urbassek, H.M. Phase transitions in an Fe system containing a bcc/fcc phase
812 boundary: An atomistic study. Phys. Rev. B **87**, 104108 (2013).
813 [64] Song, H. & Hoyt, J.J. A molecular dynamics simulation study of the velocities, mobility
814 and activation energy of an austenite-ferrite interface in pure Fe. *Acta Mater.* **60**, 4328-4335
815 (2012).
816 [65] Song, H. & Hoyt, J.J. An atomistic simulation study of the migration of an austenite-ferrite
817 interface in pure Fe. *Acta Mater.* **61**, 1189-1196 (2013).
818 [66] Lee, B.-J., Baskes, M.I., Kim, H. & Cho, Y.K. Second nearest-neighbor modified
819 embedded atom method potentials for bcc transition metals. *Phys. Rev. B* **64**, 184102 (2001).
820 [67] Ackland, G.J., Mendelev, M.I., Srolovitz, D.J., Han, S. & Barashev, A.V. Depelopments
821 of an interatomic potential for phosphorus impurities in a-iron. *J. Phys.: Condens. Matter* **16**,
822 S2629-S2642 (2004).

[68] Meyer, R. & Entel, P. Martensite-austenite transition and phonon dispersion curves of $Fe_{1-x}Ni_x$ studied by molecular-dynamics simulations. *Physical Review* B **57**, 5140-5147 (1998).

[69] Engin, C., Sandoval, L. & Urbassek, H.M. Characterization of Fe potentials with respect to the stability of the bcc and fcc phase. *Modelling and Simulation in Materials Science and Engineering* **16**, 035005 (2008).

[70] Daw, M.S. & Baskes, M.I. Embedded-atom method: Derivation and application to impurities, surfaces, and other defects in metals. *Physical Review* B **29**, 6443-6453 (1984).

[71] Drautz, R. & Pettifor, D.G. Valence-dependent analytic bond-order potential for transition metals. *Physical Review* B **74**, 174117 (2006).

[72] Ford, M.E., Drautz, R., Hammerschmidt, T. & Pettifor, D.G. Convergence of an analytic bond-order potential for collinear magnetism in Fe. *Modelling and Simulation in Materials Science and Engineering* **22**, 034005 (2014).

[73] Lee, B.-J. & Baskes, M.I. Second nearest-neighbor modified embedded-atom-method potential. *Physical Review* B **62**, 8564-8567 (2000).

[74] Bhadeshia, H.K.D.H. *Worked examples in the Geometry of Crystals* 2nd edn (The Institute of Materials, London, 2006).

[75] Stricker, M. & Weygand, D. Dislocation multiplication mechanisms – Glissile junctions and their role on the plastic deformation at the microscale.

[76] Cornide, J. *et al.* Distribution of dislocations in nanostructured bainite. *Solid State Phenomena* **172-174**, 117-122 (2011).

[77] Lambert-Perlade, A., Gourgues, A.F. & Pineau, A. Austenite to bainite phase transformation in the heat-affected zone of a high strength low alloy steel. *Acta Materialia* **52**, 2337-2348 (2004).

## Contributions

F.M. and W.A.C. designed the research, analysed the data, developed the model, discussed the

849 result, and wrote the paper. F.M. performed the atomistic simulations.

850

851 **Competing financial interests**

852 The authors declare no competing financial interests.

853

854 **Corresponding author**

855 Correspondence to: F. Maresca (francesco.maresca@epfl.ch)

856

# APPENDICES

## APPENDIX A. FURTHER COMPARISON WITH EXPERIMENTS

In Figs. 1b and 4a, we added a red line to indicate the possibility of having steps of normalized height greater than unity in the Fe-Ni-Mn steel measured by Moritani et al.[4]. Figure A.1 below shows the procedure that we followed for the identification of the interface line.

First (Fig. A.1a), we have indicated with blue circles the center of the atomic columns $[\bar{1}01]_{\mathrm{fcc}}$ and $[1\bar{1}1]_{\mathrm{bcc}}$ (3.7° degrees apart in this material) to better identify their position (they sometimes appear slightly blurred). We have considered only the atomic columns in proximity to the interface. Then, in Fig. A.1b we have isolated the pattern of blue dots (the center of the atomic columns). We have identified the $(1\bar{1}1)_{\mathrm{fcc}}$ and $(101)_{\mathrm{bcc}}$ traces in the plane of the image, considering both of them constant throughout the micrograph. This identification gives the best average match with the atomic pattern. Note that the column centers have a more regular distribution in the bcc phase as compared to the fcc phase, which can be due to HRTEM imaging artifacts. Indeed, the electron beam in Ref. 4 was aligned with the bcc phase $[1\bar{1}1]_{\mathrm{bcc}}$ direction, and $[\bar{1}01]_{\mathrm{fcc}}$ is slightly tilted according to the orientation relationship, thus showing poorer image quality. Note that the $(1\bar{1}1)_{\mathrm{fcc}}$ planes appear to have some curvature, as pointed out also in Ref. 13, and associated with the additional rotation $R_{\Delta}$ in our theory. Each trace has been placed by best approximation of the alignment of the atomic column centers. Every trace intersection falls on one atomic column, which thus sits at the boundary between bcc and fcc phases. Thus, the interface boundary is constructed with a red line connecting all atomic columns at the intersections. Finally in Figure A.1c the same red interface line is reported, with the HRTEM micrograph. Note that steps with normalized height 2 are present. This line is the same red line reported in Figs. 1b and 4a. This line deviates from the white line drawn by Moritani and co-workers[4]. There is no clear indication that Moritani et al.[4] attempted to indicate the exact interface boundary, but rather they indicated a qualitative interface between bcc and fcc characterized by steps. The observation of steps with normalized height greater than 1 has been also reported in Ref. 13, in a very similar material (see Figure 1a).

## APPENDIX B. DISCUSSION OF PREVIOUS ATOMISTIC MODELING

There is an extensive literature on atomistic modeling of the austenite-martensite interface in iron. We identify mainly two approaches in the literature. The first approach uses energy minimization (molecular statics) to obtain candidate interfaces, as exemplified by the pioneering work by Yang and Johnson[58]. Their main finding is that, for the NW orientation, interface steps are needed to obtain interface energies close to the experimental range. Similar conclusions were reached in the later work by Nagano and Enomoto[59], where both KS and NW orientations were considered. The latter work discussed the necessity of the interface ledges, consistent with HRTEM observations[4,13], but only the two limit cases of KS and NW were analyzed. Furthermore, no clear analysis of the interface defect structure was provided nor was the possibility of achieving a glissile/athermal interface demonstrated. Any such conclusions based on minimum energy arguments are not expected to be relevant for the austenite-martensite interface, which is kinetically-selected and thus need not be of low energy. As stated by Christian[15] (page 962): "In a martensitic reaction, the extra strain energy is tolerated because some degree of coherency is essential to the mechanism of transformation, and alternative forms of transformation with smaller strain energies do not take place because their rates are very much slower. The martensitic transformation thus occurs because of the existence of an easy growth mechanism, not requiring atomic diffusion, which leads to the rapid production of a new phase and a net lowering of the free energy. The question of growth mechanism is the central feature of a martensitic change and emphasizes the importance of the martensitic interface in such a reaction".

The second approach in the previous literature adopts relaxation at finite temperatures (via molecular dynamics) to study the motion of different initial interface structures. This was first done by Bos et al.[22], and later in studies by Tateyama et al.[60,61], Suiker and Thijsse[62], Wang and Urbassek[23,63] and, more recently, Ou et al.[24]. All these studies consider the motion of fcc-bcc interfaces with "flat" boundaries, i.e. without interface steps. Most of these interfaces are $(011)_{bcc} \parallel (111)_{fcc}$, except for Ref. 62 and some cases in Ref. 22 where $(011)_{bcc} \parallel (001)_{fcc}$ is

considered, which is not consistent with any measured austenite-martensite orientation relationship. When an analysis of the boundary is reported, it appears that the interface defect networks lie on the interface plane and hence resemble epitaxial semi-coherent interfaces. It is well established (e.g. Bhadeshia and Wayman[16], Section 9.4, Page 1041) that "the normal displacement of such an interface requires the thermally activated climb of the intrinsic dislocations. A martensitic interface cannot therefore be epitaxially semi-coherent". As a consequence, although glide mechanisms are sometimes reported[22], local atomic reshuffling and change of symmetries are usually observed[23, 62,63]. This is also not consistent with the martensite transformation, since long-standing and well-established literature states that "the absence of atomic interchange is confirmed by the growth of martensite at very low temperatures and by the fact that ordered phases remain ordered after transformation.… In the absence of diffusion, the atomic movements must be orderly and coordinated, and the neighbors of most atoms remain unchanged" (cf. Ref. 15, page 962). The work by Song and Hoyt[64,65], which is referred to in some of the above literature, represents an austenite-ferrite interface. Although interface steps are modeled, they are not aligned with $\langle 111 \rangle_{bcc}$ but rather with $\langle 100 \rangle_{bcc}$ ($\sim 55°$ apart) and hence not consistent with experiments[4,13], see Figures 1 and 4a in the main text. The authors of Refs. 64,65 mention that "the interphase boundary …. does not migrate by a martensitic motion" and is an austenite-ferrite boundary, and hence the results do not apply to the case of martensitic phase transformations in iron. Finally, none of the existing literature on atomistic modeling of the martensite-austenite interface in iron reports a clear identification of the interface defects (stacking faults, Burgers circuits and Burgers vectors) which are key new outcomes of the present work (Figures 4, 5 and 6 of the main text, along with Appendix E).

The brief literature survey outlined above clearly shows the need for the atomistic modeling of the interface as pursued in the present paper, which (1) is fully consistent with TEM and HRTEM experiments (both $\theta$ and $\varphi$ within the experimental KS and NW limits and correct alignment of the interface ledges), (2) shows a clear identification of the interface defect structure, and (3) demonstrates that such an interface can be glissile/athermal.

## APPENDIX C. FURTHER DETAILS ON THE VALIDATION OF Fe POTENTIAL

The MEAM-T parameterization[30] adopted here has the advantage of predicting (i) accurate BCC bulk phase properties (lattice constant, elastic constants), (ii) a stable FCC phase with accurate properties (lattice constant, elastic constants), (iii) $\Delta G_{\mathrm{fcc-bcc}}$ that is not too large (8.5 meV/atom) at T=0K and decreasing toward zero with increasing temperature, with $\Delta G_{\mathrm{fcc-bcc}}$ ~3 meV/atom at T=600K, for instance; (iv) transformation from BCC to FCC at high pressures; and (v) the accurate DFT interface for the KS case[34] ($\varphi = 0°$). Our interface involves dislocation motion, but only screws in FCC and edge segments in BCC (gliding on the $(\bar{1}01)_{\mathrm{bcc}}$ plane); thus the long-standing problem of proper description of BCC screw dislocation cores is avoided in this particular situation.

Note that the MEAM-T parameterization by Lee et al. (2012) (Ref. 30) was developed with the express purpose of studying phase transformations in iron. Lee et al.[30] present a thorough analysis of the calibrated potential performance along with the comparison against generally "better" approaches (analytic bond order potentials and DFT) and against experimental data. Not only is it shown[30] that the potential has correct behavior with respect to applied pressure (fcc more stable with increasing pressure/temperature), but also Bain paths are analyzed.

We benchmarked this potential with two other MEAM parameterizations (MEAM-p from the same paper and MEAM-0 by B.-J. Lee et al. (2001), Ref. 66), and with an existing EAM potentials (Ackland et al. (2004), Ref. 67). The other two MEAM parameterizations give the wrong pressure dependence (fcc becomes less stable with increasing pressure). The existing EAM potentials, with the exception of one by Meyer and Entel (1998), Ref. 68, are usually calibrated and tested for the bcc phase only and are unable to capture both fcc and bcc[69].

Most literature potentials for iron are based on the Embedded Atom Method (EAM)[70], which generally neglects some aspects that are needed to predict different stable crystalline configurations (bcc, fcc, hcp) in transition metals. An EAM parameterization capable of predicting the fcc to bcc phase transition was proposed by Meyer and Entel[68], though with low accuracy[69]. Alternative to EAM formulation are the bond-order potentials[33] and high-order approximations of tight binding[71];

both predict the relative bcc-fcc phase stability versus temperature. However, such formulations incur much higher computational costs without any guarantee of convergence to physically meaningful results[72]. In addition, we require a potential that has a stable fcc phase (positive stacking fault energy[31,32]). For these reasons, we have used the Modified EAM (MEAM) that is able to capture structural changes at reasonable computational costs[30,73].

## APPENDIX D – CONSTRUCTION OF THE ATOMISTIC AUSTENITE/MARTENSITE INTERFACE

The constructed atomistic interface is, in part, a natural consequence of being consistent with the experimental orientation relationship and habit plane. We have investigated a much wider range of possibilities than the case reported in the main text ($\varphi = 4.75°$), namely $\varphi = 0°$ (KS), $\varphi = 3.11°$, $\varphi = 5.21°$ (~NW), $\varphi = 5.7°$ and also $\varphi = 10°$.

Here the general method adopted to construct interfaces for different $\varphi$ is outlined. The first interface considered was $\varphi = 4.75°$. For this case only, we assumed a habit plane close to the experimental $(575)_{\mathrm{fcc}}$, which is reported most frequently in the literature[8,40]. After having developed the full theory on the basis of the defects observed for the $\varphi = 4.75°$ interface, the theory was used to select the habit planes for all other $\varphi$ values (see Table C.1 below). The correct construction of the interface is not at all trivial to achieve, and probably accounts why it was not reported earlier in spite of many other atomistic models of fcc/bcc interfaces (see Appendix B). The methodology we followed is as follows:

1. *Setting the exact orientation relationship:*

   The angle φ is chosen within the interval (0°, 5.26°), which sets the misorientation between the $[\bar{1}\bar{1}1]_{\mathrm{bcc}}$ direction and the $[\bar{1}01]_{\mathrm{fcc}}$ on the $(111)_{\mathrm{fcc}} \parallel (011)_{\mathrm{bcc}}$ plane;

2. *Setting the initial orientation of the fcc crystal*:

   (A) The $[\bar{1}01]_{\mathrm{fcc}}$ direction is first set parallel to a coordinate (Y) of the simulation box. This is of course not the only choice, but it allows to test different potential habit planes by

rotating the interface around Y. Indeed, habit planes have usually the form $(xyx)_{fcc}$ and therefore they all have the $[\bar{1}01]_{fcc}$ direction in common;

(B) The interface orientation predicted by the crystallographic theory (see main text) as a function of φ and the fcc/bcc lattice parameter ratio is assigned. We set this as the Z coordinate of the simulation box;

(C) As a consequence, the X direction is determined by the cross product of the previous two: the initial orientation of the fcc crystal in the simulation box is determined.

3. *Setting the initial orientation of the bcc crystal*:

(A) The bcc crystal needs to be oriented such that φ is observed as well as $(111)_{fcc} \parallel (011)_{bcc}$.

(B) As a consequence of 3.(A), the relative orientation of the bcc crystal with respect to the fcc crystal is determined. Therefore, the matrix $\mathbf{C_m}$ defining the parallelism relations between fcc and bcc crystals (also called "correspondence matrix", cf. Ref. 74) can be written.

(C) With $\mathbf{C_m}$, the bcc directions parallel to $[\bar{1}01]_{fcc}$, the habit plane direction Z and the fcc coordinate along X are set. Note, that contrary to the fcc directions, the bcc directions are in general irrational, and hence cannot be used directly to orient crystals in the LAMMPS[29] (which requires integer indexes). The irrational orientation thus needs to be approximated by an integer-indexed orientation. One needs to be careful not to depart too much from the orientation calculated by crystallography (e.g. 1° or 2° max.) in selecting the integer-indexed orientation.

4. *Matching fcc and bcc crystals.*

(A) Since orientations of fcc and bcc are set, it is possible to determine the period of both crystals along the X, Y and Z orientation. It is clear that each elementary period in bcc and fcc has a different length. For X and Y directions (i.e. in the habit plane), it is important that the number of periods in fcc and bcc is chosen such that the difference in total length (along X or Y) of fcc and bcc is low. Strains <5% are needed to achieve coherent interfaces with internal stresses small enough not to generate other defects or

alter phase energetics[1]). The choice of the Z coordinate for fcc arbitrary (it can be a fraction of a period), while for bcc it is necessary to have at least 1 full period to restore periodicity along Z direction. In fact, we first create a fully periodic bcc crystal in the correct orientation. Then we remove a 5 nm layer of atoms from the middle of the bcc crystal and insert a 5 nm layer of fcc in this region, which needs to be periodic along X and Y.

(B) Before minimization, it is checked that, by expanding the shorter crystal (either bcc or fcc) along X and Y, periodicity is recovered at the boundaries.

5. *Matching the interface at steps*.

Almost "perfect" matching between fcc layer and bcc needs to be ensured before minimization starts. This involves (i) removing "overlapping" atoms, (ii) removing "voids"/vacancies and (iii) setting the two crystals at a relative initial configuration that sets the initial energies of each atom at the interface to be on the same order of magnitude as the energy of the bulk fcc and bcc crystals. This avoids wild creation of defects in the bulk phases during relaxation.

6. *Selecting the interface to study*.

(A) To avoid arbitrariness in the choice of the initial relative position of bcc and fcc in the (X,Y) plane, with consequent impact on the resulting structure, the energy minimization/relaxation process is performed on a 10 x 10 grid on the (X,Y) plane, with a maximum relative shift of 1 Burgers vector (such that all possible relative configurations between bcc and fcc are probed). For each interface, minimization using

[1] Obtaining small mismatch strains (<1%) is challenging if, at the same time, one wants to achieve a reasonable simulation size. We achieved this for the $\varphi = 3.11°$ interface (reported in Section 3), where the mismatch strains along X and Y directions were 0.7% and 0.66%, respectively, and the energy difference is 10.7 meV/atom. For other interface orientations, larger strains, approaching 5%, were obtained, but these strains do not create much energy difference between fcc and bcc (and hence the driving force for transformation is not altered). For the case $\varphi = 4.75°$, the fcc-bcc difference is 11.25 meV/atom in the simulation cell as compared to 8.5 meV/atom between bulk fcc and bcc crystals at 3GPa hydrostatic pressure.

the FIRE algorithm at $10^{-3}$K is performed to very tight tolerances on both forces ($10^{-8}$) and energies ($10^{-8}$). Minimizations are then alternated with full box relaxations to a target pressure (3GPa hydrostatic stress and zero shear stresses[2]) until $10^{-15}$ tolerance. These two steps are repeated until convergence of the results, which is usually achieved after repeating the procedure 10 times.

(B) If all previous steps are correct, the initial interface will not equilibrate until the fcc phase is fully consumed. The consumption of the fcc phases happens via gliding of the interface dislocations in glissile manner. There is no reshuffling of atoms except during the initial steps of equilibration to form the interface structure. Some initial configurations can emit defects into the bulk phases. In order to study the process of interface motion, without including further complications, we selected the interface which has the minimum energy configuration among those (1) not moving spontaneously during equilibration and (2) not emitting defects close to the interface itself.

7. *Remarks.*

(A) *The choice of the angle φ*. To our understanding, the most delicate part involves the selection of an angle φ such that the bcc orientation is described by "reasonably low" indexes to obtain periodicity with "small" simulation boxes (involving mismatich strains <5%). In general, unless the KS orientation is adopted, higher φ are preferable for computations since they lead to lower-index bcc orientations, and hence more tractable simulation box sizes. This drove the initial choice of $\varphi = 4.75°$, which corresponds to $[\bar{5}\bar{6}6]_{bcc} \parallel [\bar{1}01]_{fcc}$ . The selection of $[232]_{fcc}$ habit plane, which is just 2° from that suggested by experiments, was made on the basis of the necessary size of the periodic simulation box.

[2] The 3 GPa case models martensite growth in a constrained environment. Glissile interfaces are obtained also at zero applied hydrostatic stress. The interface defect structure does not depend on the applied hydrostatic stresses, see Appendix F.

(B) Note that points 1. and 2. can be exchanged, namely the bcc crystal can be first set into position (and hence $[\bar{1}\bar{1}1]_{\mathrm{bcc}}$ parallel to Y and the habit plane close to $(\bar{1}54)_{\mathrm{bcc}}$) and the fcc orientation determined after φ is fixed. We also tried this and obtained analogous results as when fcc orientation is taken as reference.

While constructing interfaces at various $\varphi$, we found that if the correct habit plane is not selected (e.g. if we attempt to enforce the $(575)_{\mathrm{fcc}}$ habit plane for all orientations) then the interface emits defects into the bulk phases. With the correct habit plane, the qualitative interface defect structure does not change with $\varphi$. The interfaces only differ in the spacing of the bcc screw dislocations and the average interface orientation. Table D.1 shows the habit plane estimated by the theory, compared with the habit plane adopted for calculations.

| **Interface** | **Predicted habit plane** | **Interface orientation simulations** | **fcc orientation** | **bcc orientation** |
|---|---|---|---|---|
| $\varphi = 0°$ (KS) | 2.7° from $(121)_{\mathrm{fcc}}$ | $(121)_{\mathrm{fcc}}$ | X ∥ $[\bar{1}1\bar{1}]_{\mathrm{fcc}}$<br>Y ∥ $[\bar{1}01]_{\mathrm{fcc}}$<br>Z ∥ $[121]_{\mathrm{fcc}}$ | X ∥ $[\bar{5}1\bar{4}]_{\mathrm{bcc}}$<br>Y ∥ $[\bar{1}\bar{1}1]_{\mathrm{bcc}}$<br>Z ∥ $[\bar{1}32]_{\mathrm{bcc}}$ |
| $\varphi = 3.11°$ | 1.26° from $(10\ 17\ 10)_{\mathrm{fcc}}$ | $(10\ 17\ 10)_{\mathrm{fcc}}$ | X ∥ $[\overline{17}\ 20\ \overline{17}]_{\mathrm{fcc}}$<br>Y ∥ $[\bar{1}01]_{\mathrm{fcc}}$<br>Z ∥ $[10\ 17\ 10]_{\mathrm{fcc}}$ | X ∥ $[\bar{9}2\bar{6}]_{\mathrm{bcc}}$<br>Y ∥ $[\bar{8}\bar{9}9]_{\mathrm{bcc}}$<br>Z ∥ $[\overline{36}\ 129\ 97]_{\mathrm{bcc}}$ |
| $\varphi = 4.75°$ | $(2\ 3\ 2)_{\mathrm{fcc}}$ | $(2\ 3\ 2)_{\mathrm{fcc}}$ | X ∥ $[\bar{3}\ 4\ \bar{3}]_{\mathrm{fcc}}$<br>Y ∥ $[\bar{1}01]_{\mathrm{fcc}}$<br>Z ∥ $[2\ 3\ 2]_{\mathrm{fcc}}$ | X ∥ $[\overline{18}\ 5\ \overline{10}]_{\mathrm{bcc}}$<br>Y ∥ $[\bar{5}\bar{6}6]_{\mathrm{bcc}}$<br>Z ∥ $[\overline{30}\ 158\ 133]_{\mathrm{bcc}}$ |
| $\varphi = 5.21°$ (NW) | 1.2° from $(232)_{\mathrm{fcc}}$ | $(232)_{\mathrm{fcc}}$ | X ∥ $[\bar{3}4\bar{3}]_{\mathrm{fcc}}$<br>Y ∥ $[\bar{1}01]_{\mathrm{fcc}}$<br>Z ∥ $[232]_{\mathrm{fcc}}$ | X ∥ $[\overline{33}\ 8\ \overline{19}]_{\mathrm{bcc}}$<br>Y ∥ $[\bar{9}\ \overline{11}\ 11]_{\mathrm{bcc}}$<br>Z ∥ $[\overline{121}\ 534\ 435]_{\mathrm{bcc}}$ |
| $\varphi = 5.7°$ | 0.9° from $(575)_{\mathrm{fcc}}$ | $(575)_{\mathrm{fcc}}$ | X ∥ $[\bar{7}\ 10\ \bar{7}]_{\mathrm{fcc}}$<br>Y ∥ $[\bar{1}01]_{\mathrm{fcc}}$<br>Z ∥ $[575]_{\mathrm{fcc}}$ | X ∥ $[\overline{15}\ 4\ \bar{8}]_{\mathrm{bcc}}$<br>Y ∥ $[\bar{4}\bar{5}5]_{\mathrm{bcc}}$<br>Z ∥ $[\overline{20}\ 107\ 91]_{\mathrm{bcc}}$ |
| $\varphi = 10°$ | n.a. | $(575)_{\mathrm{fcc}}$ | X ∥ $[\bar{7}\ 10\ \bar{7}]_{\mathrm{fcc}}$<br>Y ∥ $[\bar{1}01]_{\mathrm{fcc}}$<br>Z ∥ $[575]_{\mathrm{fcc}}$ | X ∥ $[\overline{15}\ 3\ \bar{7}]_{\mathrm{bcc}}$<br>Y ∥ $[\bar{2}\bar{3}3]_{\mathrm{bcc}}$<br>Z ∥ $[\overline{12}\ 59\ 51]_{\mathrm{bcc}}$ |

**Table D.1** | **Interfaces constructed.** Geometric data for all interfaces constructed in this work.

## APPENDIX E. DETAILS ON THE IDENTIFICATION OF INTERFACE SCREWS

Identification of the $\frac{a_{\mathrm{bcc}}}{2}[1\bar{1}1]$ Burgers vector in Figs. 6a, 7a-d and 8b is rather straightforward. It is done by drawing the Burgers circuit far from the dislocation core and by identifying the failure in circuit closure as the Burgers vector. In contrast, identification of the Burgers vector of $\frac{a_{\mathrm{fcc}}}{2}[\bar{1}01]$ screw dislocations and the demonstration that the screw dislocations are not on every $(111)_{\mathrm{fcc}}$ plane but can be at a spacing $\geq 1$ normalized height, is less straightforward.

We perform the rigorous identification of $\frac{a_{\mathrm{fcc}}}{2}[\bar{1}01]$ screw dislocations in the KS case, where $\varphi = 0°$ and thus edge defects are absent, and the interface structure is cleaner (see Fig. 8a). To this end, we calculate the screw and edge components of the atomic displacements after the interface has moved with differential displacement maps between two configurations: (1) a configuration with the fcc-bcc interface and (2) a configuration where the fcc layer has partially transformed into bcc. By comparison, we can identify the displacement field due to the motion of the interface dislocation cores, as shown in Figure E.1.

The screw components are dominant (see Figure caption for interpretation of the arrow magnitudes, for both edge and screws). For the KS case, the interface dislocations are positioned at the interface between fcc and bcc, because for this specific orientation the slip plane and direction of screws are the same in both phases. The presence of edge components dominantly along the $(111)_{\mathrm{fcc}}$ direction demonstrates the presence of partials, although for KS the core might be more compact than for other orientations because of the coincidence with bcc, as the Volterra analysis below shows. This demonstrates that hcp atoms shown in Fig. 6a and Figs. 7a-d indicate a stacking fault, which is a characteristic feature of screws in fcc. The screw displacement fields are present on 2 interplanar spacings out of 3. This justifies the theory, which accounts for steps of normalized height $\beta \geq 1$. There is one screw dislocation per step, and thus $\beta = 1.5$ for KS configuration (our theory prediction yield $\beta = 1.4$). Thus, for the KS orientation relationship, $[\bar{1}01]_{\mathrm{fcc}}$ screw dislocations are present at the interface and their spacing is equal or greater than one $(111)_{\mathrm{fcc}}$ interplanar spacing.

We further show in Figure E.2 that the Burgers vector of these defects is $[\bar{1}01]_{\mathrm{fcc}}$ by comparing

atomic positions at the interface with the prediction of elasticity theory (the Volterra solution). Figure E.2a identifies the atoms at the interface where change of symmetry from fcc to bcc is observed, while proceedings on each interplanar spacing, along the $(111)_{\mathrm{fcc}}$ planes. Figure E.2b isolates such atoms and envisions them in an initial, undeformed configuration. We then imagine inserting a cut plane in Fig. E.2b coming from the bcc phase and ending in the middle of the atom cluster. We then identify uniquely atoms A-E via the angle $\alpha$ (positive clockwise) measured from the end of the cut plane. Inserting a Volterra field with center at the tip of the cut plane yields the displacement field $u(\alpha) = \frac{b\alpha}{2\pi}$, with $b = 2.50$ Å the fcc Burgers vector. The displacements are calculated for each atom, and the final positions are obtained by taking as reference atom B and assigning the initial position 5.26 Å, as in the simulations. The difference between atomic positions estimated with the Volterra solution and the simulations is shown in Table E.1, and is about 0.1b, except for atom A (~0.2b). This is consistent with the fact that the dislocation core is not as compact as assumed in the Volterra solution, and thus atomic relaxations show slightly lower relative displacements between atoms than that predicted with the Volterra solution.

| Atom | Angle | Volterra displacement $u(\omega)$ | Position (Volterra) | Position (Simulations, spacing 1) | Position (Simulations, spacing 3) | Position difference |
|---|---|---|---|---|---|---|
| A | $\alpha_A \simeq -\frac{5}{6}\pi$ | $-\frac{5}{12}b$ | 5.68 Å | 6.14 Å | 6.22 Å | $0.18b - 0.22b$ |
| B | $\alpha_B \simeq -\frac{\pi}{6}$ | $-\frac{b}{12}$ | 5.26 Å | 5.26 Å | 5.26 Å | - |
| C | $\alpha_C \simeq \frac{\pi}{6}$ | $\frac{b}{12}$ | 5.68 Å | 5.45 Å | 5.45 Å | $0.09b$ |
| D | $\alpha_D \simeq \frac{\pi}{2}$ | $\frac{b}{4}$ | 7.34 Å | 7.03 Å | 7.04 Å | $0.12b$ |
| E | $\alpha_E \simeq \frac{5}{6}\pi$ | $\frac{5}{12}b$ | 6.51 Å | 6.23 Å | 6.25 Å | $0.10b - 0.11b$ |

**Table E.1 | Comparison between Volterra solution and simulations.**

To summarize, the analysis shows that the atomic positions at the interface are consistent with the presence of $\frac{a_{\mathrm{fcc}}}{2}[\bar{1}01]$ screw dislocations, with spacing equal to 1 or 2 $(111)_{\mathrm{fcc}}$ interplanar distances.

## APPENDIX F – SPECIFIC DETAILS OF THE $\varphi = 4.75°$ INTERFACE

In this section, we demonstrate the details of the construction of the $\varphi = 4.75°$ interface (analyzed in the main text) and show that the interface structure is equivalent to a perfectly glissile interface. We also demonstrate that hydrostatic pressure does not change the interface structure, but can influence the relative energy of bcc and fcc phases.

The austenite-martensite bicrystal analyzed in the main text, having $(232)_{\mathrm{fcc}}$ interface orientation, has been constructed by assigning the following orientations for the two phases with respect to the global $(X, Y, Z)$ cartesian coordinates of the simulation cell:

1) fcc: X $\parallel$ $[\bar{3}4\bar{3}]_{\mathrm{fcc}}$, Y $\parallel$ $[\bar{1}01]_{\mathrm{fcc}}$ and Z $\parallel$ $[232]_{\mathrm{fcc}}$ ;

2) bcc: X $\parallel$ $[\overline{18}\ 5\ \overline{10}]_{\mathrm{bcc}}$, Y $\parallel$ $[\bar{5}\bar{6}6]_{\mathrm{bcc}}$ and Z $\parallel$ $[\overline{30}\ 158\ 133]_{\mathrm{bcc}}$.

The dimensions of the simulation cell are $L_X = 6.3$ nm, $L_Y = 5.5$ nm and $L_Z = 59.5$ nm. This yields an initial misorientation of approximately 1.8° between the closed-packed planes $(111)_{\mathrm{fcc}}$ and $(011)_{\mathrm{bcc}}$. This value falls within the experimental measurements based on electron back scattered diffraction (EBSD) analysis, see Figure 4a in Ref. 11.

During the relaxation of the bicrystal, a defect is emitted from the interface into the bcc phase, to accommodate the misorientation between the two closed-packed planes. The result is that the two closed-packed planes are nearly parallel at the interface. This is consistent with transmission electron diffraction (TEM) analysis at the martensite-austenite interface by Kelly et al.[10]. The resulting interface has $(111)_{\mathrm{fcc}} \parallel (011)_{\mathrm{bcc}}$ and $[\bar{1}\bar{1}1]_{\mathrm{bcc}}$ misoriented by $\varphi = 4.75°$ with respect to $[\bar{1}01]_{\mathrm{fcc}}$ on the $(111)_{\mathrm{fcc}}$ plane, which falls within experimental measurements (e.g. Fig.3c in Ref. 10).

By considering different initial relative configurations of fcc with respect to bcc, a stable configuration can be found while relaxing the bicrystal, and hence the minimum interface energy can be calculated and phase transformation under applied deformation can be studied.

The interface energy is 530 mJ/m$^2$, in the range of experimental measurements and previous atomistic simulations[58,59]. Note that the interface is kinetically selected, and hence need not be minimum energy. Indeed, the minimum energy configuration corresponds to the KS case, which is

not glissile. The structural differences of this interface as compared to other interfaces that are perfectly glissile, and hence which glide until the whole fcc layer is consumed, is undetectable. Movie 1 shows the motion of one interface steps on the $(111)_{fcc}$ plane, starting from configuration Fig. F.1d. Movie 2 shows the motion of the interface starting from configuration Fig. F.1b. The interface structure does not change, and hence motion is mediated by the cooperative gliding of the interface defects.

A perfectly glissile bicrystal with a $(575)_{fcc}$ habit plane has also been constructed. Note that the experimental habit plane is between $(575)_{fcc}$ and $(232)_{fcc}$, which are misoriented by $\sim 2°$. To achieve this, the following orientations are adopted for the two phases with respect to the global $(X, Y, Z)$ cartesian coordinates of the simulation cell:

1) fcc: X $\parallel$ $[\bar{7}\ 10\ \bar{7}]_{fcc}$, Y $\parallel$ $[\bar{1}01]_{fcc}$ and Z $\parallel$ $[575]_{fcc}$ ;

2) bcc: X $\parallel$ $[\overline{18}\ \ 5\ \overline{10}]_{bcc}$, Y $\parallel$ $[\bar{5}\bar{6}6]_{bcc}$ and Z $\parallel$ $[\overline{30}\ 158\ 133]_{bcc}$.

The dimensions of the simulation cell are $L_X = 25.2$ nm, $L_Y = 5.5$ nm and $L_Z = 59.5$ nm (4x larger than the previous cell). The initial thickness of the fcc phase is 5 nm. This yields $(111)_{fcc} \parallel (011)_{bcc}$ and $\varphi = 4.75°$ with respect to $[\bar{1}01]_{fcc}$ on the $(111)_{fcc}$ plane, from the start. No emission of defects within the bulk phases occurs.

A snapshot of the interface during equilibration (T=0K) is reported in Fig. F.1a. The bicrystal with $(232)_{fcc}$ interface is shown for comparison in Fig. F.1b. Figs. F.1c,d show a typical $(111)_{fcc}$ interface ledge of the $(575)_{fcc}$ interface, belonging to a non-equilibrium configuration occurring during equilibration, and the ledge of the $(232)_{fcc}$ interface.

We show now that, although the Fig. F.1c snapshot is taken on a non-equilibrated crystal (the interface continuously moves), it is representative of the $(575)_{fcc}$ interface. One way this interface can be stabilized is to apply a larger hydrostatic pressure.

A stable interface is achieved under a pressure of 25 GPa, above the 18GPa pressure at which fcc and bcc phases have same enthalpy. A typical $(111)_{fcc}$ interface ledge of the 25 GPa $(575)_{fcc}$ interface is shown in Fig. F.2a. The cut is taken on the same $(111)_{fcc}$ plane as for the 3 GPa $(575)_{fcc}$

interface, see Fig. F.2b. Since the structure of the $(575)_{fcc}$ interface does not noticeably change by varying pressure, and since the 25 GPa interface is an equilibrium configuration, we conclude that the structure of the $(232)_{fcc}$ interface is equal to the structure of the $(575)_{fcc}$ interface. This also demonstrates that applying a hydrostatic pressure does not change the interface structure.

Having shown that the $(232)_{fcc}$ interface has same features as the $(575)_{fcc}$ interface, we now show that the differences between them are almost undetectable. In the $(232)_{fcc}$ interface, due to the higher interface misorientation with respect to $(111)_{fcc}$ ledges as compared to the $(575)_{fcc}$ interface, some steps are narrower. One such step is shown in Fig. F.3a, to be compared with a typical step (Fig. F.3b). The character of the defects (Burgers vector, spacing) is the same, but the local crystalline symmetry changes slightly due to the difference in ledge size.

The $(232)_{fcc}$ interface can also show a "defective" ledge, as seen in Fig. F.3c. The ledge is similar in size to the narrow interface ledge analyzed in Fig. F.3a On the defective ledge, the $a_{bcc}/2\ [1\bar{1}1]$ edge-character kink cores are shifted with respect to each other, and not aligned along $[\bar{1}01]_{fcc}$. Also, the spacing slightly changes, from regular 2.55 nm to irregular with a smaller distance of 2.35 nm. A similar defective ledge, with irregular spacing and misaligned edge-character kink defects, is also found in a $(232)_{fcc}$ glissile interface that is unstable (Fig. F.3d).

Therefore, there are only some undetectable local differences in atomic arrangements that inhibit the spontaneous propagation of the interface. This explains the very low stress (less than 1 MPa) needed (at T=0K) to initiate interface propagation, which is thus demonstrably athermal. Note also that not all glissile $(232)_{fcc}$ interfaces have such defective step, and such cases have the same structure as $(575)_{fcc}$ except for the presence of some narrower steps.

## APPENDIX G. STRUCTURE OF INTERFACES OVER A RANGE OF TEMPERATURES

According to the long-standing theory of martensite transformation (e.g. Christian[15], chapters 21, 22 and 23), temperature does not influence the intrinsic interface motion, aside from the obvious need to quench the material to provide the thermodynamic driving force for the fcc to bcc transformation. This

transformation is diffusionless, requiring no local atomic rearrangements/reshuffling and no thermal activation. As stated by Bhadeshia and Wayman, "The fact that martensite can grow at low temperatures and high velocities means that the transformation interface must be very mobile and be able to move without any need for diffusion. The interface must be *glissile*" (Bhadeshia and Wayman (2014), Ref. 27, page 1041). We have verified that our interfaces, constructed at T=0K and demonstrably glissile and athermal, preserving the same structure at finite temperatures up to T=600K.

The interface structures at different temperatures for the case $\varphi = 4.75°$ are shown in Fig. G.1. No changes occur in terms of defect structure: all interfaces are equivalent and hence independent of temperature. Local changes in CNA labeling, which are only visible at T = 600K are due solely to the amplitudes of atomic vibrations, and do not change the interface defect structure. Over a simulation time of 50 picoseconds, in the absence of applied stress/deformation, the interfaces do move from their initial positions. No reshuffling is observed, and the movement is mediated by the coordinate gliding of the interface defects, as at T=0K. With increasing temperature from 0K to 600K, the Gibbs free energy difference decreases from 8.5 meV down to ~3 meV (see Lee et al.[1], Figure 8). Hence, in spite of the very small thermodynamic driving force at T=600K, the interface moves. All these observations further confirm the glissile nature of the constructed interface.

## APPENDIX H. DETAILS ON ATOMIC DISPLACEMENTS DURING TRANSFORMATION

The displacement pattern in Fig. 9c shows that the $[\bar{1}01]_{\mathrm{fcc}}$ component of the displacement field is developed within the interface region, due to the glide of the screws. This pattern is representative of 4 out of the 6 $(111)_{\mathrm{fcc}}$ planes that cross the interface. The pattern of the two remaining planes is shown in Fig. H.1a,b.

It is clear, in both Figs. H.1a and H.1b, that sliding is first activated at $[1\bar{1}1]_{\mathrm{bcc}}$ to preserve coherency followed by the start of a change in local symmetry from fcc towards bcc. The final bcc configuration with the homogeneous displacement along $[\bar{1}01]_{\mathrm{fcc}} + 19.5°$ degrees direction is achieved, in the plane,

almost without the gliding of the $[\bar{1}01]_{\mathrm{fcc}}$ defects. This means that the two planes do not glide completely relative to the neighboring planes, along $[\bar{1}01]_{\mathrm{fcc}}$. This is consistent with the theory, with $\beta = 1.5$.

Figs. H.1c,d shows the atomic displacement components along the two defects, on the $(111)_{\mathrm{fcc}}$ plane analysed in Figure 9c. The defects with Burgers vector along $[1\bar{1}1]_{\mathrm{bcc}}$ show a displacement jump on the $(111)_{\mathrm{fcc}}$ plane. A careful analysis of the displacement jump shows that this is mostly limited to the interface region. Within this region, the edge-character kinks are in bcc orientation, and not in fcc. However, the final bcc phase, and hence the full lattice transformation, is accomplished after the slip of the edge-character kinks.

The identification of the $(\bar{1}01)_{\mathrm{bcc}}$ glide plane for the $[1\bar{1}1]_{\mathrm{bcc}}$ defects is a bit more subtle. Fig. H.2a shows the interface viewed on the $(\bar{1}01)_{\mathrm{bcc}}$ plane, close to $(\bar{1}11)_{\mathrm{fcc}}$ plane.

This was assumed in the theory as the glide plane for the bcc screw defects. Although displacement jumps are visible between most $[1\bar{1}1]_{\mathrm{bcc}}$ columns of atoms on the $(\bar{1}01)_{\mathrm{bcc}}$ planes, some atoms on neighboring planes move together (center of Fig. H.2a). Therefore, the $[1\bar{1}1]_{\mathrm{bcc}}$ defects are edge-character kink segments gliding on $(\bar{1}01)_{\mathrm{bcc}}$ planes.

A further confirmation of the fact that $(\bar{1}01)_{\mathrm{bcc}}$ is the slip plane is obtained by analyzing the atomic displacements. Specifically, unlike X and Y components, the Z component of the atomic displacements depends only on the product $\boldsymbol{S} = \boldsymbol{R} \cdot \boldsymbol{B}$ and the shear $\boldsymbol{P}^{(2)}$ due to the $[1\bar{1}1]_{\mathrm{bcc}}$ defects. The first term contributes $\sim 2\%$ deformation due to the change in interplanar spacing, which in fcc is $1/\sqrt{3}$ Å $\simeq 0.58$ Å. This yields, on each plane, a displacement $d_{p,Z} \simeq 0.011$ Å. The shear of the $[1\bar{1}1]_{\mathrm{bcc}}$ defects produces a displacement along Z because it lies on the $(011)_{\mathrm{bcc}}$ plane, which is rotated of $\theta$ with respect to $Z \parallel (011)_{\mathrm{bcc}}$ around $Y \parallel [\bar{1}01]_{\mathrm{fcc}}$. The latter is $\sim 60°$ from $[1\bar{1}1]_{\mathrm{bcc}}$. The component of $b = a_{\mathrm{bcc}}/2[1\bar{1}1]$ perpendicular to Y axis is $b_{\perp} \simeq \frac{\sqrt{3}}{2} \cdot \frac{a_{\mathrm{bcc}}}{2}[1\bar{1}1] \simeq$ 2.14 Å. This yields a maximum Z-displacement on each plane equal to $d_{s,Z} = b_{\perp} \cdot \sin\theta \simeq 0.423$ Å. Therefore, since $d_{s,Z} \sim 40\, d_{p,Z}$, we conclude that any Z displacement due to the transformation is almost completely due to the shear $\boldsymbol{P}^{(2)}$. Hence, this displacement component must be due to a

shear along the slip plane of $\boldsymbol{P}^{(2)}$. This is shown in Fig. H.2b, where the displacement jump due to the edge-character kinks follows the initial alignment of these defects, which do not lie on the same $(\bar{1}01)_{\mathrm{bcc}}$ plane.

## APPENDIX I. NEW CONDITIONS FOR GLISSILE/ATHERMAL MOTION

The concept of a glissile/athermal interface, i.e. no thermal activation, no diffusion, and high velocity, is at the foundations of the theory of martensite crystallography[15,16,28]. Our new fcc-bcc interface is glissile/athermal but with a structure that relaxes previous hypothesized conditions for such an interface. We can thus revise prior conditions.

Theory[15,16,28] posits three conditions for a glissile/athermal interface[16] based on the idea that any interface defects must glide and carry the transformation in a cooperative manner to avoid creation of jogs that would pin the interface. Condition 1 is that the intrinsic dislocations are either screw or have Burgers vectors not lying in the interface plane; this ensures that the defects reach the interface by gliding. Condition 2 is that the glide planes in fcc and bcc of the intrinsic dislocations must meet edge-to-edge in the interface; this ensures that the defects do not get pinned at the interface but can migrate into the other phase and carry the transformation. Condition 3 is that the two sets of intrinsic dislocations should have either the same line vector in the interface or parallel Burgers vectors; then, the interface can move as an integral unit without creation of pinning jogs. No existing theory fully complies with all three conditions.

The atomistic interface has steps aligned with $[\bar{1}01]_{\mathrm{fcc}}$, and adjacent screw dislocations having $a_{\mathrm{fcc}}/2[\bar{1}01]$ Burgers vector and gliding on $(111)_{\mathrm{fcc}}$; this is consistent with previous assumptions. However, we find edge-character kink segments at the interface with $a_{\mathrm{bcc}}/2\,[1\bar{1}1]$ Burgers vector (associated with immobile screws) that glide on $(\bar{1}01)_{\mathrm{bcc}}$, but they cannot cross the interface at the $[\bar{1}01]_{\mathrm{fcc}}$ steps. This was not explicitly envisioned by any previous theories. Moreover, the presence of straight screw dislocations in fcc (KS case),

although consistent with Conditions 1 and 2 above, provides a glissile mechanism, but does not ensure athermal motion. These defects thus appear to be not fully consistent with the three Conditions above.

However, Condition 1 is met by both sets of intrinsic dislocations. However, the athermal nature of the motion is due to the presence of kinks in at least one set of screws, otherwise the interface motion requires thermal activation. Furthermore, Condition 2 is only met by the $a_{fcc}/2[\bar{1}01]$ dislocations. The Burgers vector, line direction, and slip plane of the $a_{bcc}/2\,[1\bar{1}1]$ dislocations in the bcc phase are all misoriented with respect to their counterparts in the fcc phase. But, since Condition 2 ensures the propagation of defects between the parent and the product phases, it is relevant only for the $[\bar{1}01]_{fcc}$ screws that carry the step/interface, triggering the transformation (as demonstrated in Section 3). The second set of defects needs only to be confined to the ledges behind the steps, since gliding in bcc restores compatibility with the neighboring fcc phase. Finally, Condition 3 is not met by the atomistic interface but is too restrictive. At the interface, the $a_{bcc}/2[1\bar{1}1]$ edge-character kinks remain in the bcc phase and cannot cross the $[\bar{1}01]_{fcc}$ screws at the interface even if they do not share line vector/Burgers vector with the fcc screws. As clarified above and by the analysis of the $\varphi = 0°$ interface, self-pinning (via bcc kinks crossing the fcc screws) is prevented by the fact that slip planes and dislocation line direction do not coincide in bcc and fcc for the bcc dislocations. Therefore, Condition 3 is sufficient but not necessary for a glissile interface, as also implied in Ref. 28, and is only necessary if one set of dislocations *could* cross the other into the fcc phase. We thus provide a less-stringent interpretation of the long-established conditions for a glissile interface: the glissile interface satisfies Conditions 1 and 2 appropriately only due to the existence of one set of dislocations defects and does not need to satisfy Condition 3. Moreover, athermal motion is ensured only if at least one set of defects has edge-character kinks.

Our theory also predicts the possibility that the step line deviates from $[\bar{1}01]_{fcc}$, thus

generating edge-character kinks on the fcc screws. In the presence of kinks on both sets of screws (expected mainly for Fe-C alloys), the mechanism of motion might be affected, in the sense that first the fcc kinks need to "unzip", moving the fcc screw to the next Peierls valley, and at a second stage the bcc kinks move to accommodate for the angle $\varphi$. This mechanism would probably affect the propagation speed of the interface (which was not addressed in the present paper). When fcc screw segments are ahead of the bcc kinks, we can envision the same local geometry as shown in the atomistic interfaces simulated here (Fig. 7). We cannot exclude a priori possible reaction of fcc and bcc kinks when the former aligns with the slip direction of the latter; but if the reaction occurs, it would result in a glissile junction[75], since the Burgers vector of bcc kinks belongs to the intersection of the two slip planes of the dislocations involved in the reaction, i.e. $(111)_{\mathrm{fcc}} \parallel (011)_{\mathrm{bcc}}$ and $(\bar{1}01)_{\mathrm{bcc}}$, and the glide system of the glissile junction results in $(111)_{\mathrm{fcc}} \parallel (011)_{\mathrm{bcc}}$ with Burgers vector equal to the vector sum of $\frac{a_{\mathrm{fcc}}}{2}[\bar{1}01]$ and $\frac{a_{\mathrm{bcc}}}{2}[1\bar{1}1]$. Also, the glissile/athermal interface structure predicted by the present theory might break down at smaller angles, closer to NW ($\varphi \geq 5.26°$) because of edge-character kinks in bcc crossing the fcc screws at the interface due to increased alignment of the corresponding slip systems in fcc and bcc phases with increasing $\varphi$.

## APPENDIX J. POSSIBLE RELEVANCE TO BAINITE

Bainite in steels forms at higher temperature than lath martensite, and can show a similar microstructure with carbon-depleted ferritic laths and carbon supersaturated austenite layers. Fig. J.1 shows the comparison of the atomistic interface with HRTEM micrographs in Ref. 4 on ferritic bainite-austenite interfaces. The match between atomic rows is again good. Ref. 4 reports the same sets of defects as for lath martensite-austenite interface, namely (i) steps aligned with $[\bar{1}01]_{\mathrm{fcc}}$ and related screws and (ii) a second set of defects with Burgers vector $a_{\mathrm{bcc}}/2[1\bar{1}1]$. The main difference lies in the habit plane orientation, close to $(252)_{\mathrm{fcc}}$, namely more inclined with respect to

$(111)_{fcc}$ than in lath martensite. This is visible from the comparisons between atomistic simulations and experiments in Fig. J.1a.

Since the bainitic transformation is at least partially displacive[76,77], and since the bainitic ferrite-austenite interface presents the same characteristics as the lath martensite-austenite interface, the assumptions of present paper can be taken as the basis of the crystallographic theory of martensitic transformation applied to bainite reactions. Note that the phenomenological theory of martensitic transformation has been used for predictions of variants and transformation deformation (e.g. Ref. 77). In Ref. 77, the choice of the order of the invariant shears $\boldsymbol{P}^{(2)}$ and $\boldsymbol{P}^{(3)}$, as well as the definition of the invariant shear systems normals and directions, are based on Ref. 18. Thus, systems not complying with the experimental interface are considered. The application of the crystallographic theory as proposed in the present paper to bainite is justified by the bainite-austenite interface defect structure, as shown in Fig. J.1. Results might differ from previous analyses.

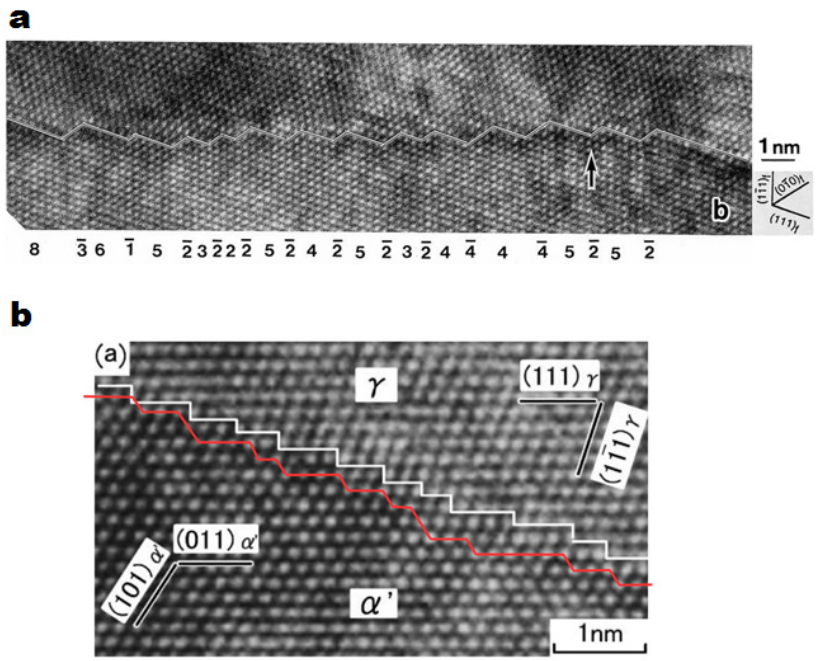


**Figure 1 | HRTEM structure of the fcc-bcc interface.** fcc-bcc interfaces in Fe-Ni-Mn steels showing steps along the $[\bar{1}01]_{fcc}$ direction, a habit plane oriented at angle θ with respect to $(111)_{fcc}$, and varying step heights. **a**. Fe-Ni-Mn with the interface indicated by white segments and where numbers with overbars indicate the (normalized) step height. Reproduced from Ref. 13 with permission of Taylor & Francis. **b**. Fe-Ni-Mn with interface atoms connected by a red line, again showing multiple step heights. The authors of the micrograph indicated the interface as a white line with single step height. The red line is constructed by careful drawing of the traces of $(1\bar{1}1)_{fcc}$ and $(101)_{bcc}$ for all atomic rows in the micrograph, followed by connecting the intersection points of these two trace families (see Appendix A for the explicit construction). The micrograph from Ref. 4 is reproduced with the permission from Elsevier.

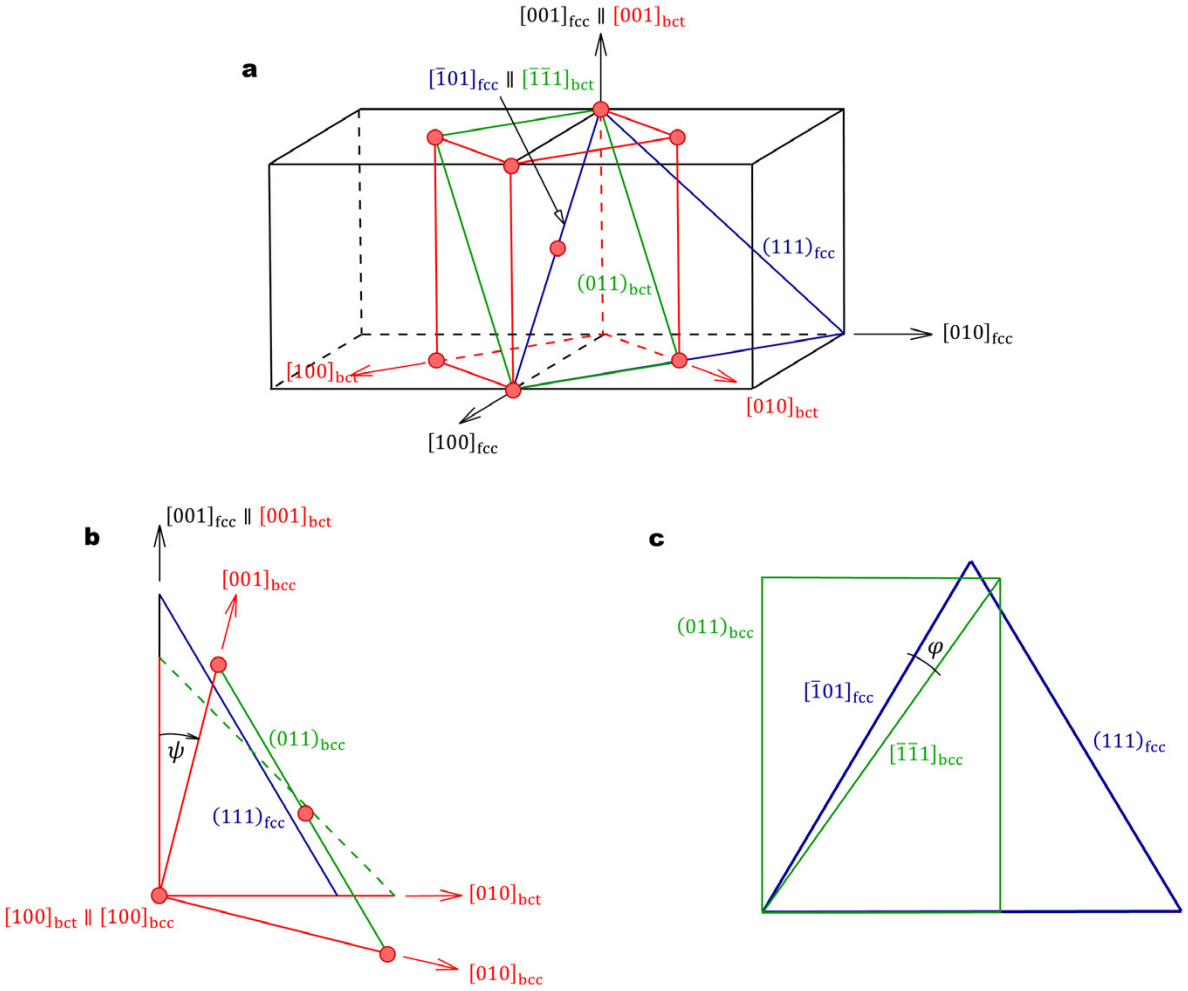


**Figure 2 | Transformation path from the fcc austenite lattice to the bcc martensite lattice.** **a.** The Bain strain $\boldsymbol{B}$ transforms the fcc unit cell, which can be viewed as a body-centered-tetragonal (bct) structure, into the bcc unit cell; the resulting bcc structure is then misoriented with respect to the fcc. **b**. The rotation $\boldsymbol{R}_{\psi}$ by the angle $\psi$ around $[100]_{\mathrm{bcc}}$ aligns $(111)_{\mathrm{fcc}} \parallel (011)_{\mathrm{bcc}}$, and gives the NW orientation relationship ($\varphi_{NW} = 5.26°$). **c**. The rotation $\boldsymbol{R}_{\varphi}$ by the angle $\omega = \varphi_{NW} - \varphi$ around $[111]_{\mathrm{fcc}} \parallel [011]_{\mathrm{bcc}}$ leads to the final experimental orientation relationship at the interface, which lies between KS ($\varphi = 0°$) and NW ($\varphi = 5.26°$).

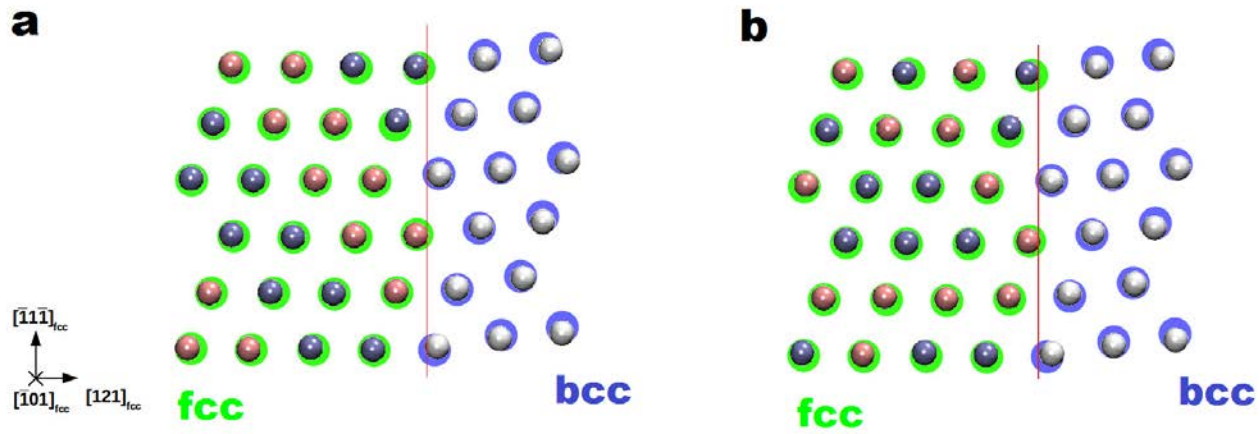


**Figure 3 | Comparison of KS interface structure as predicted by DFT and the MEAM-T potential.** Overlay of DFT-computed[34] atomic positions (shaded atoms) on the MEAM-T-computed atomic positions (flat-colored atoms) For DFT, shaded red and shaded dark blue atoms belong to fcc (red = spin up; blue = spin down), while shaded silver indicate atoms belonging to bcc. For MEAM-T, flat green indicates atoms belong to fcc, while flat blue atoms belong to bcc. Straight red lines indicate the average $(121)_{fcc}$ habit plane. **a**, Comparison between MEAM-T computations and DFT with AFMD magnetic configuration for fcc. **b**, Comparison between MEAM-T computations and SQS magnetic configuration for fcc. The interface energy predicted by the MEAM-T potential is 390 mJ/m$^2$, very close to the DFT values (410 mJ/m$^2$ for AFMD and 450 mJ/m$^2$ for SQS magnetic configurations).

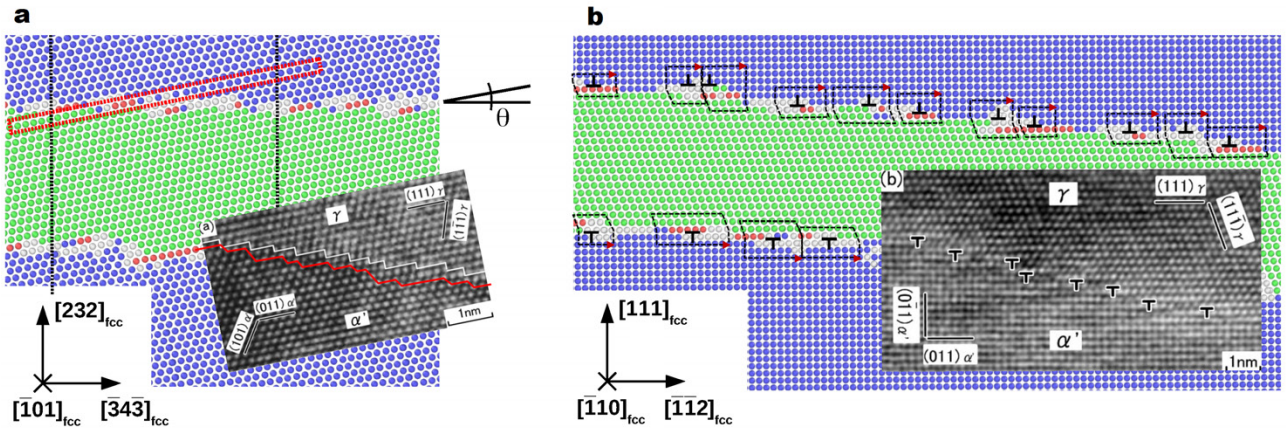


**Figure 4 | Comparison between simulated and experimental[4] interfaces. a**, View along $[\bar{1}01]_{fcc}$. The angle θ between $(111)_{fcc}$ plane and the average interface orientation (habit plane) is indicated. Dashed black lines indicate the simulation cell boundaries. The red rectangle indicates the portion of $(111)_{fcc} \parallel (011)_{bcc}$ plane analyzed in Figure 6a. The red line indicates the atomic positions where corresponding $(1\bar{1}1)_{fcc}$ and $(101)_{bcc}$ plane traces meet, accurately delineating the interface as compared to the white line drawn in the original work (see Appendix A). The red line shows that the fcc/bcc interface consists of steps of different heights (here, one or two $(111)_{fcc}$ interplanar distances). **b**, View along $[\bar{1}10]_{fcc}$; the interface dislocations are indicated by Burgers circuits and the associated Burgers vector. Burgers circuits are around interface ledges and are constructed with respect to reference, unstrained crystals, according to Hirth[35]. Crystallographic visualizations use OVITO[36] and adaptive Common Neighbor Analysis (CNA)[37] to assign colors to atoms with fcc (green), bcc (blue), hcp (red) and other (grey) according to the local atomic environment; CNA is not sufficiently precise to discern detailed local structure and defects. Micrographs are from Ref. 4 and are reproduced with the permission from Elsevier.

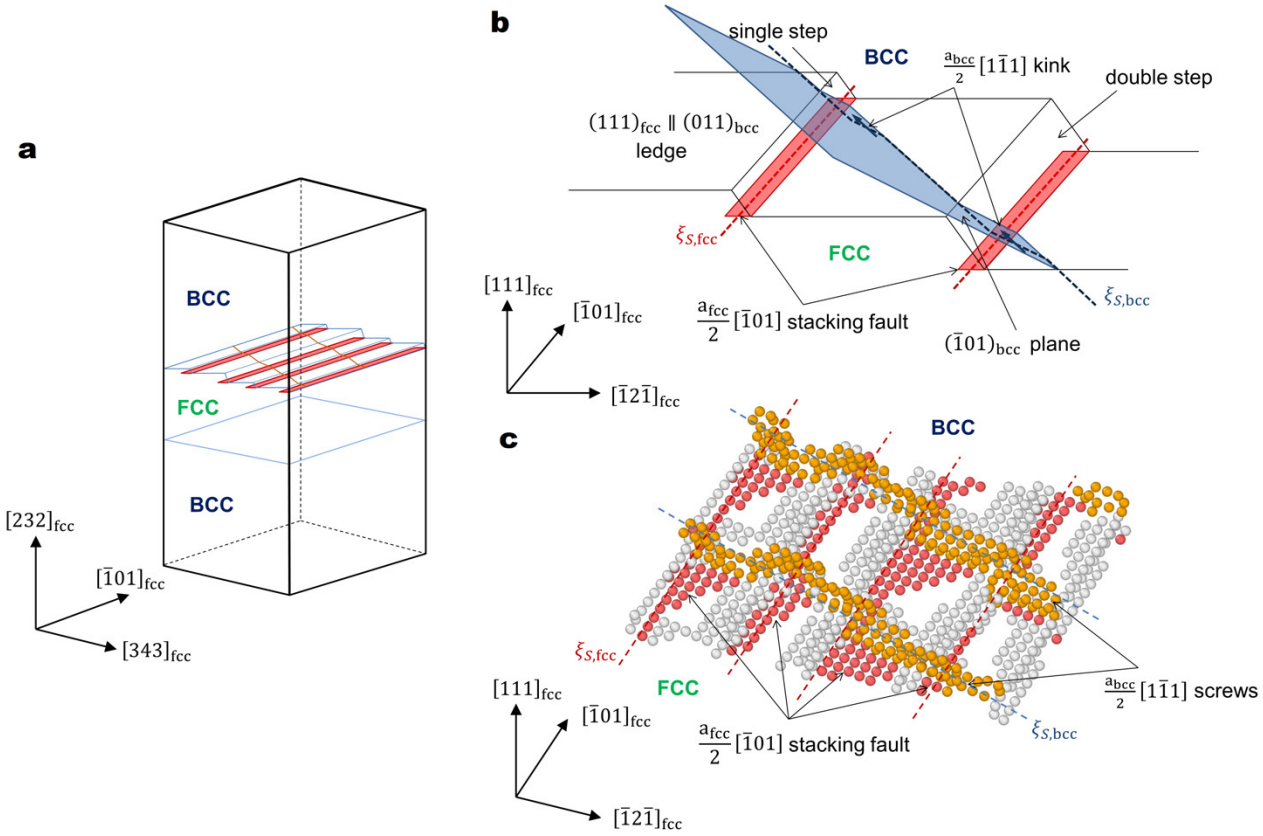


**Figure 5 | Interface defect structure. a**, View of the simulation box with the two bcc-fcc interfaces. The interface defect structure (steps, stacking faults, bcc screws) is indicated in the top interface. **b**, Zoom-in of the 3D interface structure, showing interface single and double steps, fcc stacking faults, dislocation line directions ($\xi_{S,\mathrm{fcc}}$ and $\xi_{S,\mathrm{bcc}}$), kinks on bcc screws and slip planes. **c**, View of the interface structure for the case $\varphi = 4.75°$. Only the atoms which are not in either fcc or bcc local symmetry according to CNA[37] are visualized. Red color indicates hcp atoms (and hence the stacking fault associated with fcc screws). Orange atoms indicate the bcc screws. Grey are not indexed atoms.

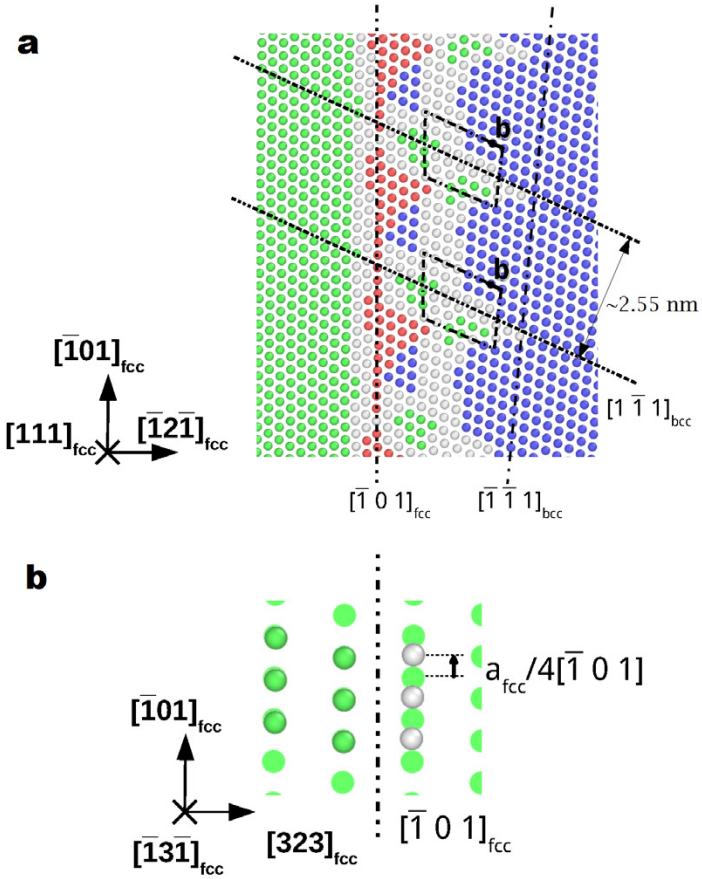


**Figure 6 | Burgers vectors of interface defects. a**, Interface structure along the $(111)_{fcc} \parallel (011)_{bcc}$ crystallographic habit plane. The line directions of the defects, Burgers vectors, and $[1\bar{1}1]_{bcc}$ defects spacing are indicated. The Burgers vector of the $[1\bar{1}1]_{bcc}$ dislocations is indicated, at the kinks (having edge character). Colors show local atomic environment according to CNA[37]. **b**, Half-Burgers vector of the $[\bar{1}01]_{fcc}$ screws measured on the $(\bar{1}3\bar{1})_{fcc}$ plane at the interface, along the $[\bar{1}01]_{fcc}$ trace (indicated in Figure 6a). The atoms are superposed on a reference fcc crystal (flat colored green). See Appendix E for the detailed identification of the Burgers vector.

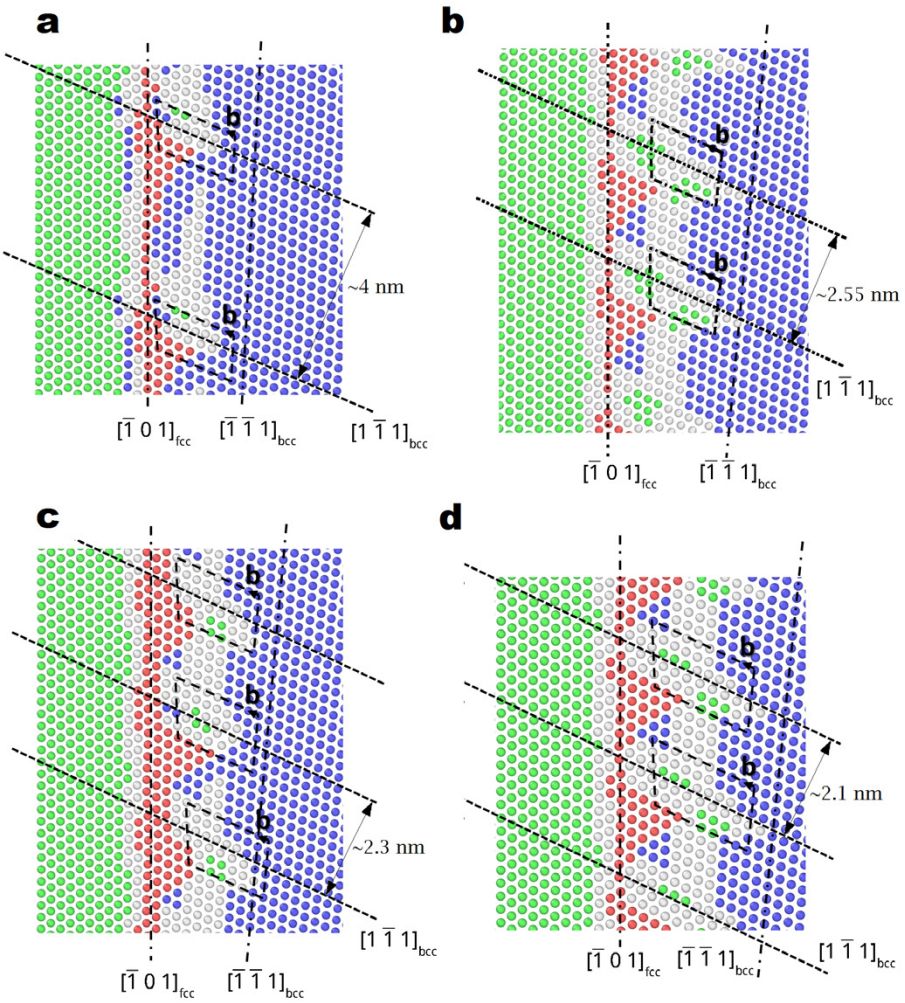


**Figure 7 | Simulated interface structures at various φ within/near the experimental range.** **a**, $\varphi = 3.11°$. **b**, $\varphi = 4.75°$, the case studied in detail in Figures 4 and 6. **c**, $\varphi = 5.21°$ (~NW orienatation). **d**, $\varphi = 5.7°$. Colors show local crystalline configurations according to CNA[37]. All interfaces in/near the experimental range ($\varphi = 3.11°, 5.21°, 5.7°$) have the same pair of defect types only the spacing changes.

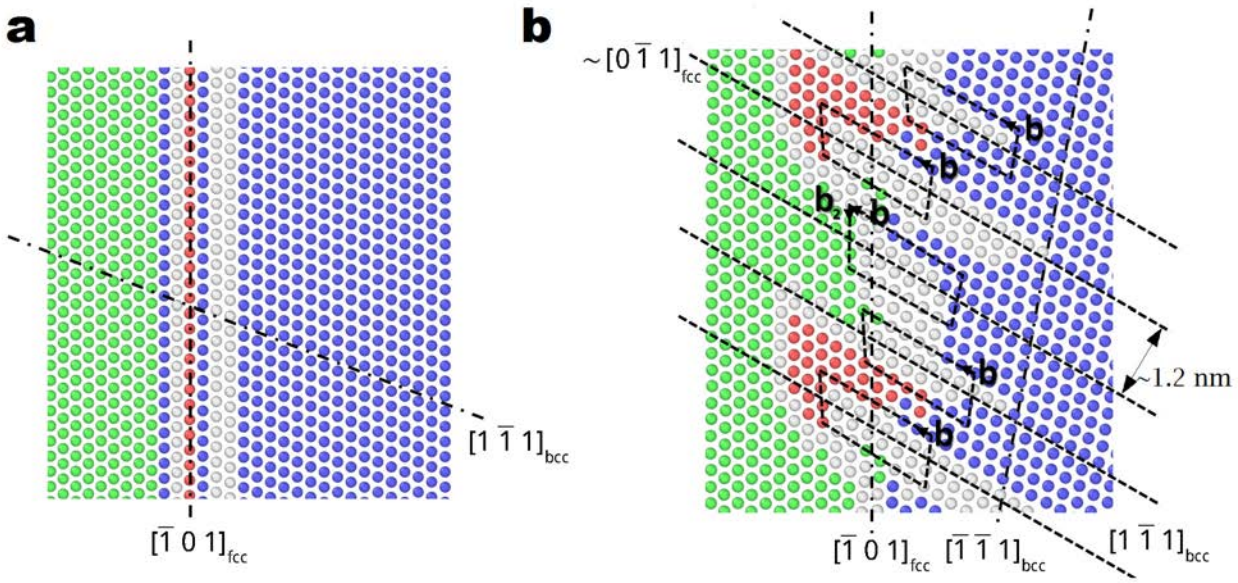


**Figure 8 | Simulated interface structures at KS orientation and at φ outside the experimental range.** **a**, $\varphi = 0°$ (KS orientation). **b**, $\varphi = 10°$. Colors show local crystalline configurations according to CNA[37]. Interface with KS orientation or outside the experimental range ($\varphi = 0°, 10°$) show a fundamentally different structure than those in Figure 7.

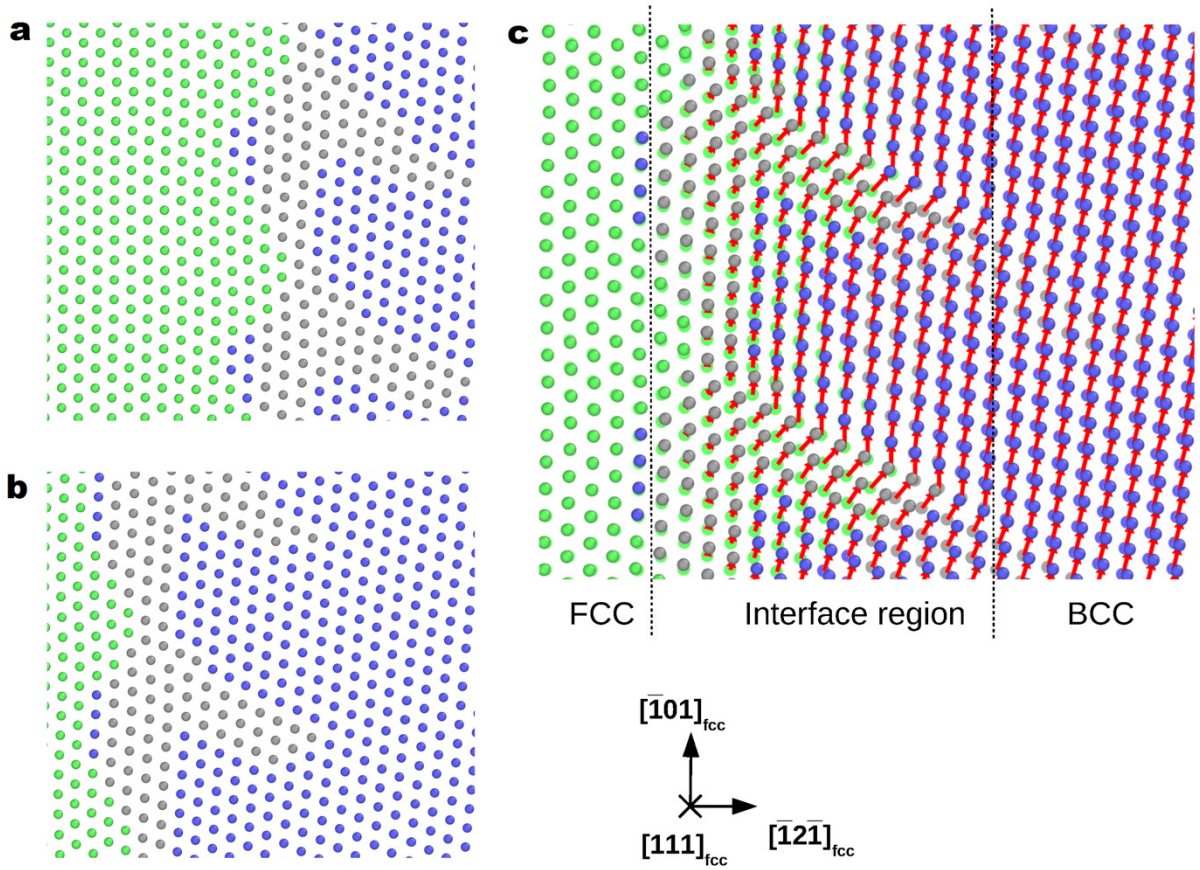


**Figure 9 | Motion of the interface. a**, Interface structure on one $(111)_{fcc}$ plane before applying any deformation. **b**, Interface structure on the same plane after deformation at an applied stress of 1 MPa. **c**, Atomic displacements at the interface on one $(111)_{fcc}$ plane; the deformed configuration is superposed over the initial configuration (flat colored atoms) and red arrows connect initial and final atom configurations. See text for discussion. Colors show local atomic environment according to CNA[37]. Two movies of the gliding motion are provided in Appendix H.

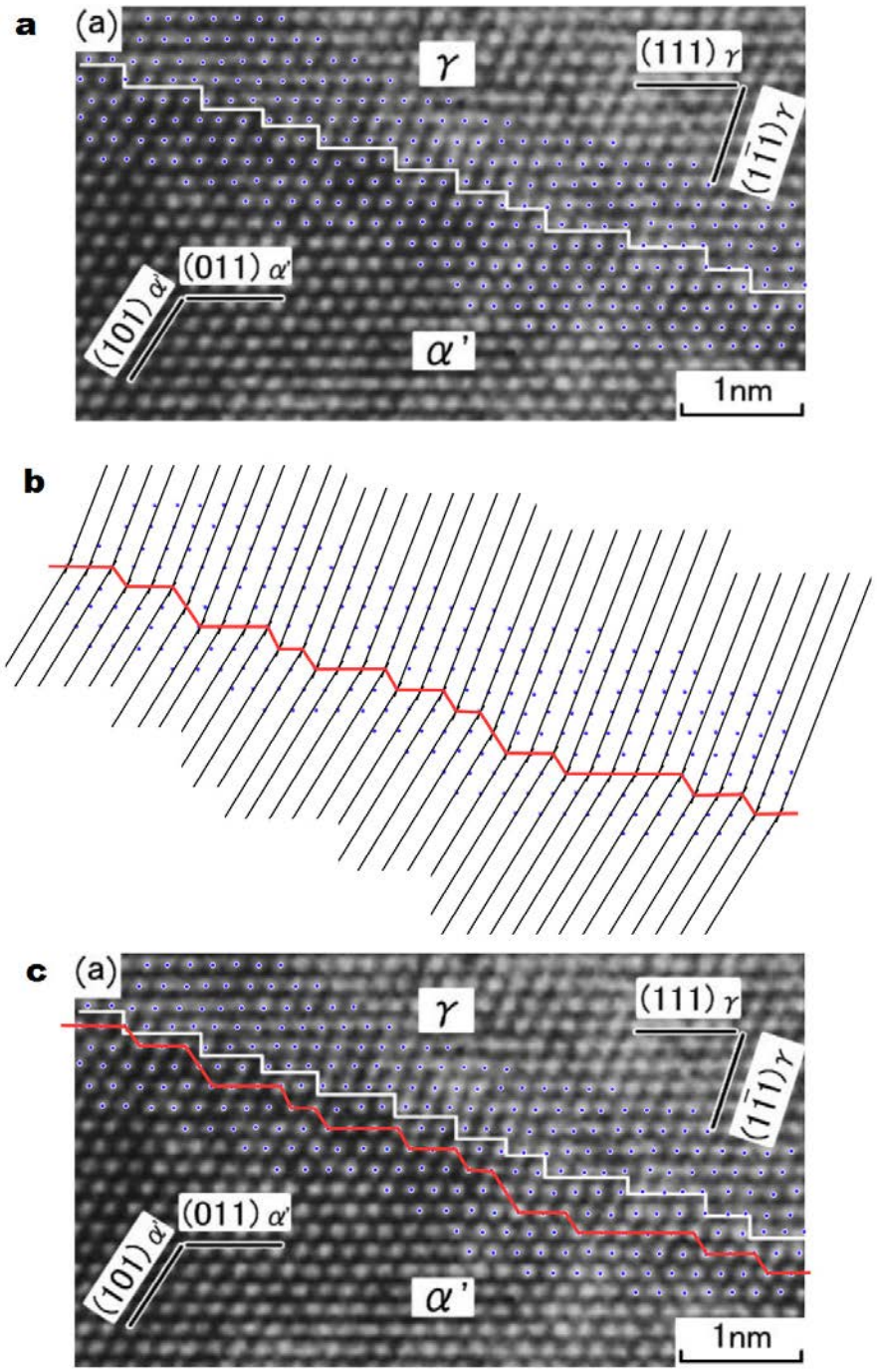


**Figure A.1 | Interface identification in Moritani et al.[4] HRTEM micrograph. a**, identification of the center of atomic columns near the interface (indicated with blue circles). **b**, identification of intersection points between $(1\bar{1}1)_{fcc}$ and $(101)_{bcc}$ plane traces. The red line connects all point of intersections between these traces. Each point of intersection sits on an atomic column which is in common between fcc and bcc lattices. **c**, the same red line is reported on the original micrograph.

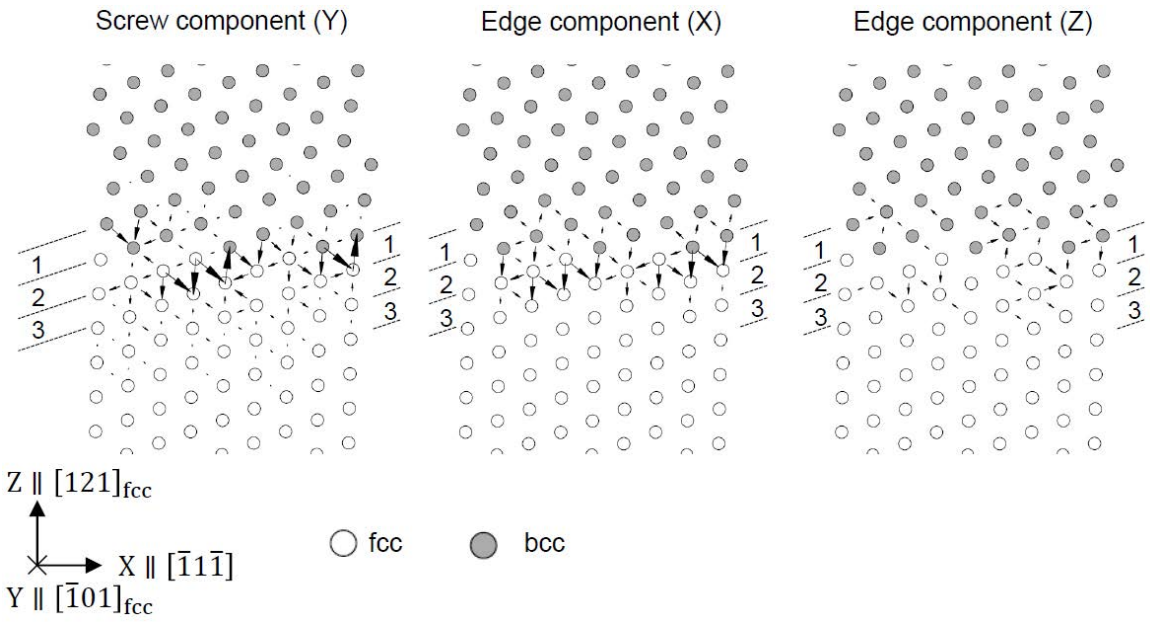


**Figure E.1 | Differential displacement plots of interface $[\bar{1}01]_{fcc}$ screws.** The plots are made on a periodic unit cell, with 3 $(111)_{fcc}$ planes crossing the interface (numbers indicate the 3 interplanar spacings). The screw components, which are present only at interplanar spacings 1 and 3 (consistent with the theory with $\beta = 1.5$) and are in the fcc phase, indicate the relative displacement between neighboring atoms along the $[\bar{1}01]_{fcc}$ direction, with respect to a reference bcc configuration. The magnitude of the arrows is $\frac{b}{2}$ if they connect the center of two atoms. For ease of visualization, both edge components are normalized such that an arrow connecting the center of two neighboring atoms has length $\frac{a_{fcc}}{12}[112]$. Edge components are dominant along X direction, consistent with the presence of two partials with a stacking fault in between (as visualized with OVITO[36]).

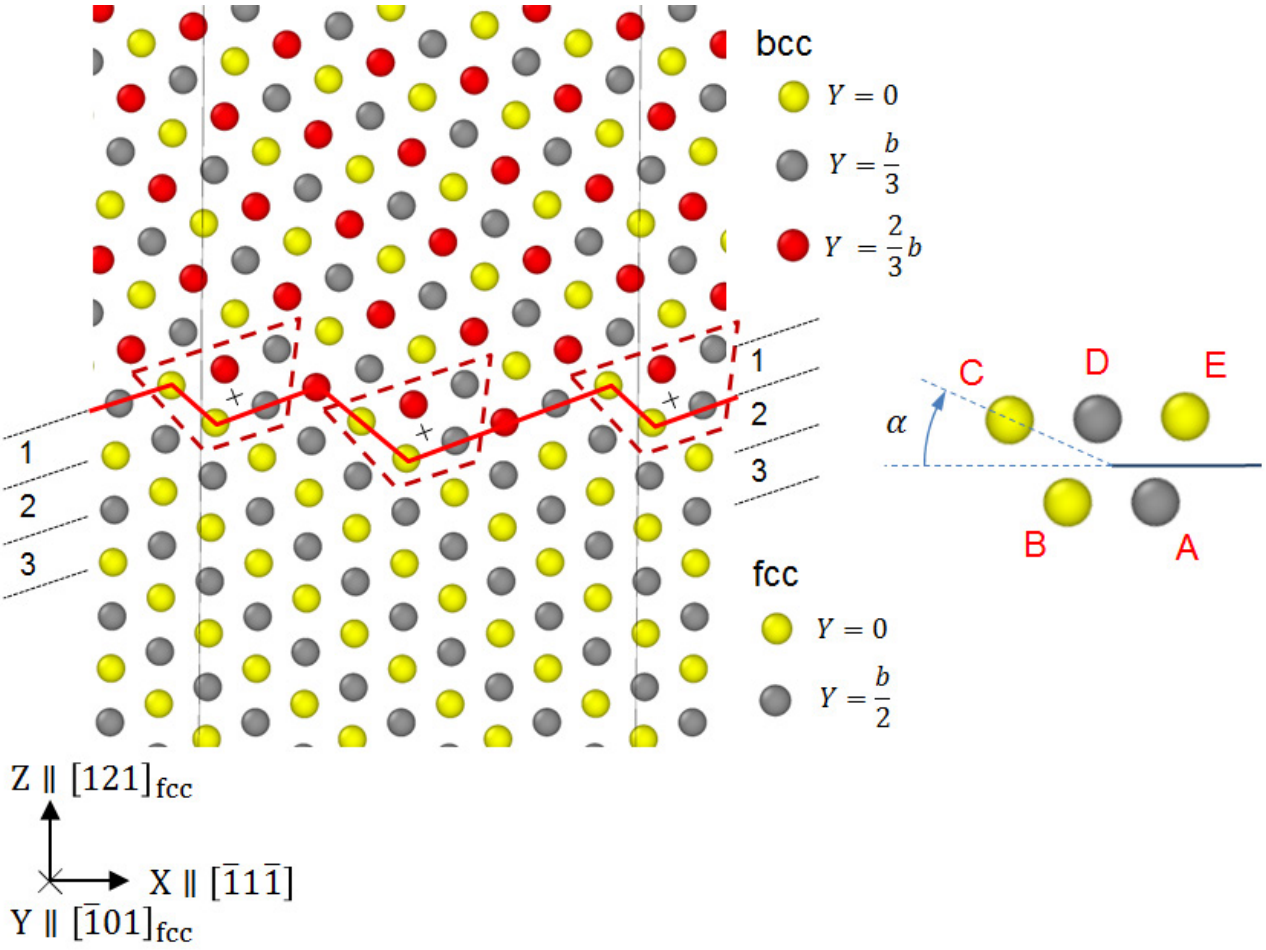


**Figure E.2 | Calculation of Volterra displacement field associated with interface screws. a**, Representation of atomic stackings in $\langle\bar{1}01\rangle$ fcc zone axis and $\langle\bar{1}\bar{1}1\rangle$ bcc zone axis. The atomic positions related to different colors are indicated in the figure. They are taken in the relaxed bicrystal and thus the values indicated for fcc and bcc are approximate. The same silver color is assigned to $Y = b/3$ in bcc and $Y = b/2$ in fcc, because these two atomic planes tend to join at the interface. The interface between fcc and bcc is indicated by a continuous red line. Dashed lines indicate the interface atoms where the passage from fcc to bcc stacking is accomplished, and they are present in interplanar spacings 1 and 3 (where screws are identified, see Figure E.1). Black crosses indicate the position of the dislocation core. **b**, The atoms identified by the dashed red line in Fig. E.2.a are now imagined in a reference fcc crystal, and their positions are labeled for computing the Volterra field. Angle $\alpha$, which is taken positive in the clockwise direction, identifies uniquely each atomic position.

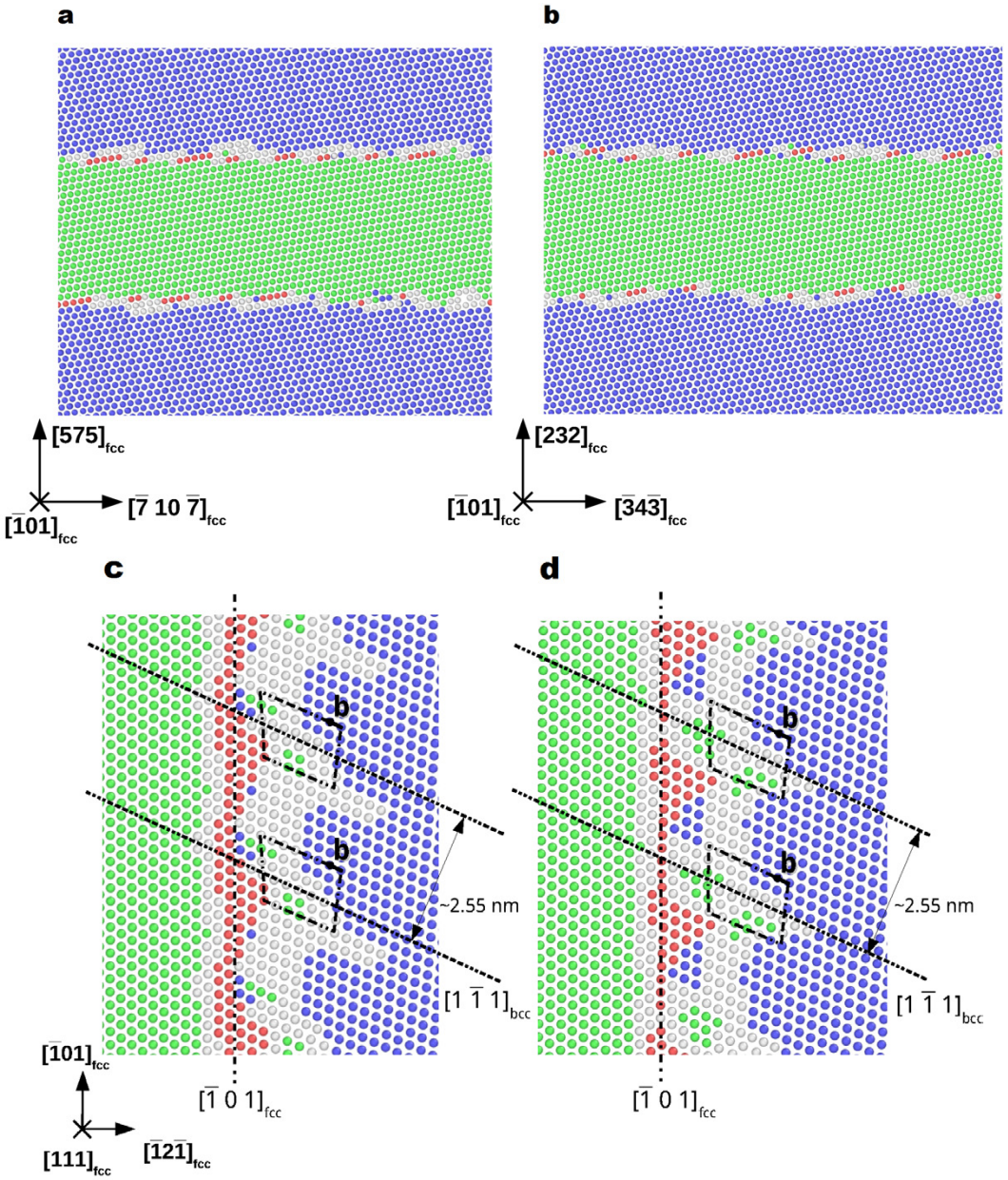


**Figure F.1 | Comparison of bicrystals with different interface orientation. a**, View of the bicrystal with $(575)_{fcc}$ interface (during relaxation). **b**, View of the bicrystal with $(232)_{fcc}$ interface. **c**, A typical $(111)_{fcc}$ ledge of the $(575)_{fcc}$ interface. **d**, A typical $(111)_{fcc}$ ledge of the $(232)_{fcc}$ interface. Crystallographic visualizations use OVITO[36]. Colors show local crystalline configurations according to CNA[37].

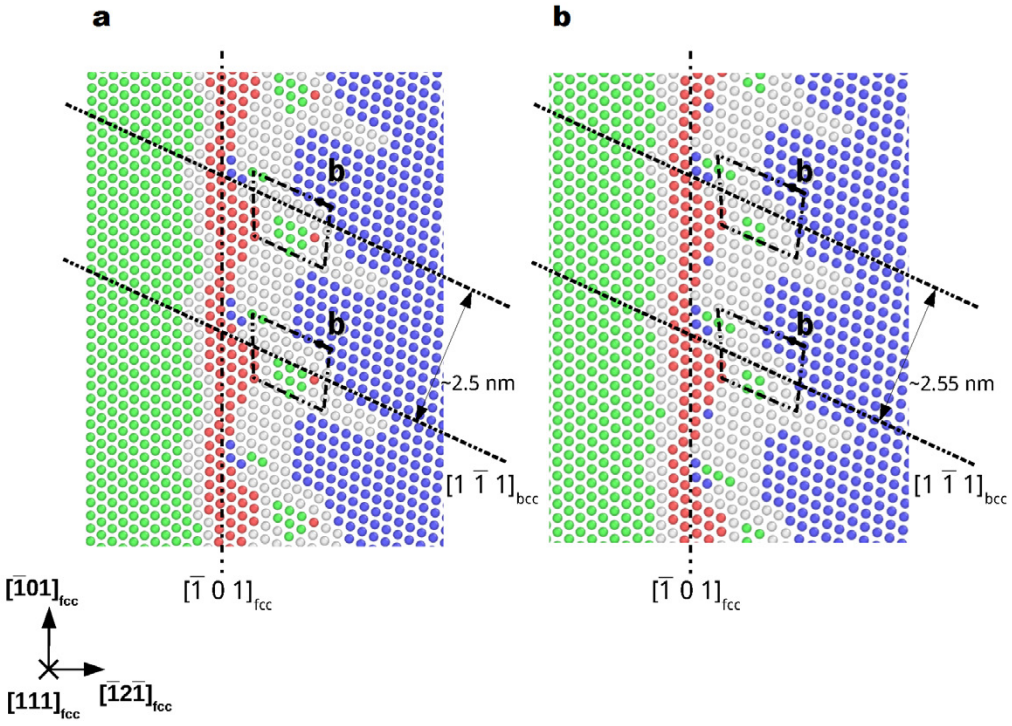


**Figure F.2 | Comparison of defect structure of $(575)_{fcc}$ interfaces with different applied pressure. a**, $(111)_{fcc}$ ledge at 25GPa applied hydrostatic pressure, after relaxation. **b**, $(111)_{fcc}$ ledge at 3GPa pressure, during relaxation. Colors show local crystalline configurations according to CNA[37].

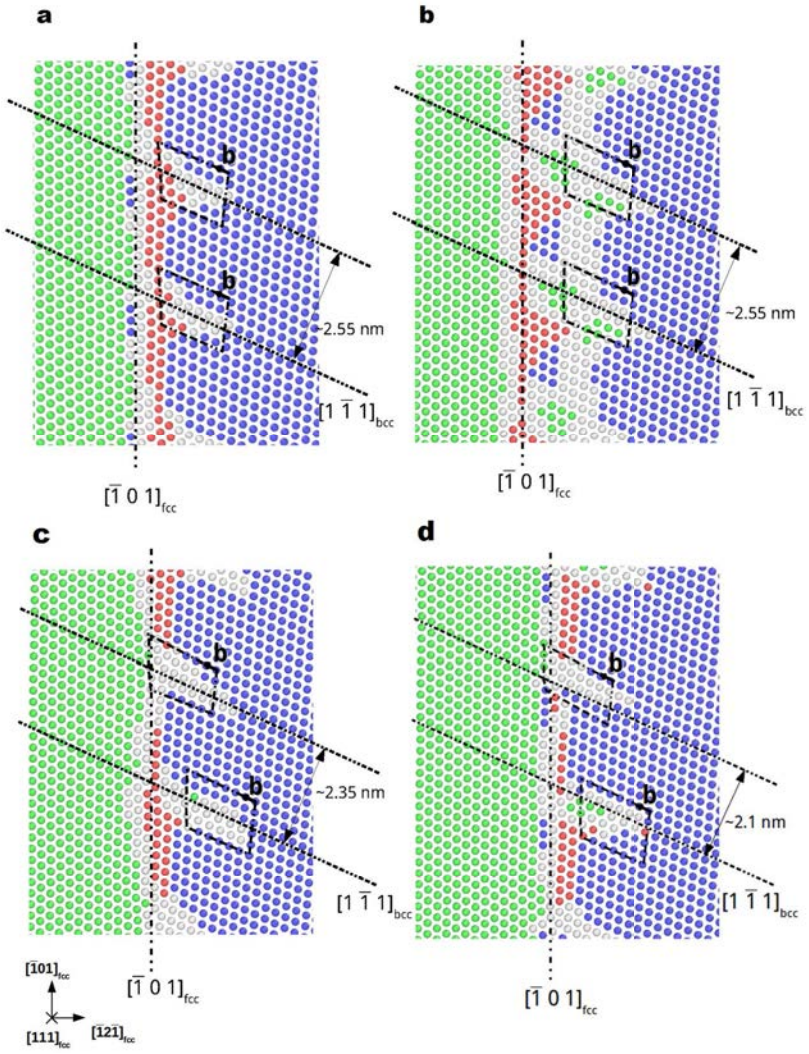


**Figure F.3 | Comparison between $(111)_{fcc}$ ledges in the $(232)_{fcc}$ bicrystal having different width and defective ledges.** **a**, ledge narrower than typical. **b**, typical ledge in the $(232)_{fcc}$ bicrystal. **c**, The defective ledge of the $(232)_{fcc}$ interface analyzed in this study. **d**, The defective ledge of a $(232)_{fcc}$ glissile interface. Colors show local crystalline configurations according to CNA[37].

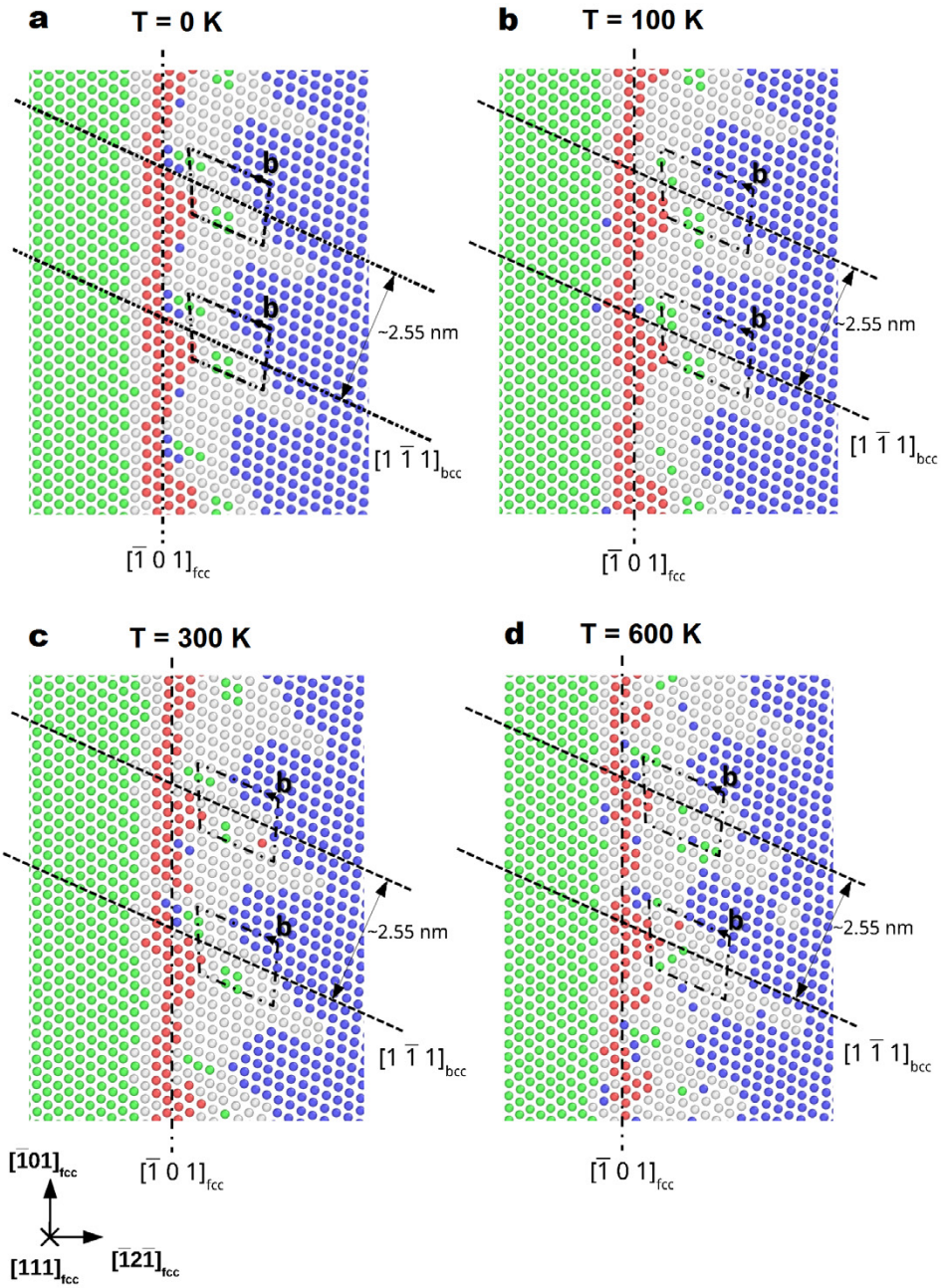


**Figure G.1 | Interface defect structure at various temperatures. a**, T = 0K. **b**, T = 100K. **c**, T = 300K. **d**, T = 600K. All snapshots are taken after 50 ps of relaxation of the $(575)_{fcc}$ glissile interface with $\varphi = 4.75°$ (Appendix F). These results show that the defects reported for T=0K are stable at all these temperatures. Colors show local crystalline configurations according to CNA[37]; increasing temperature and associated thermal vibrations leads to some apparent disorder in any instantaneous snapshot of the atomic configuration.

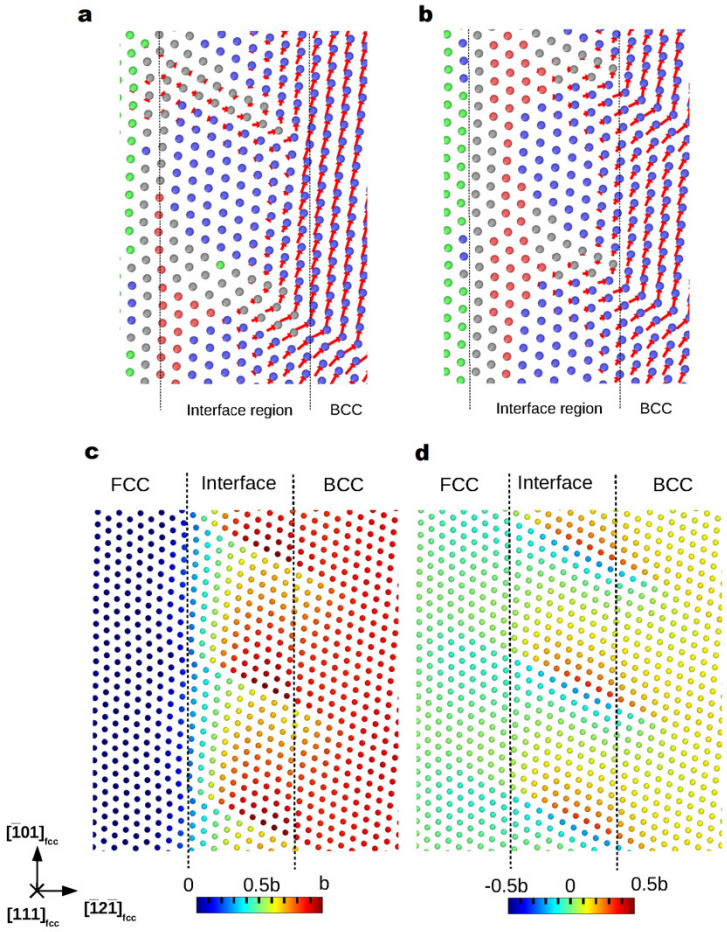


**Figure H.1 | Details on atomic displacements. a**,**b**, Atomic displacements at the interface, on the two $(111)_{fcc}$ planes not following the pattern shown in Figure 9c. Only the deformed configuration is shown. Red arrows indicate the atomic displacements. Colors show local crystalline configurations according to CNA[37]. **c**, Atomic displacement component along $[\bar{1}01]_{fcc}$ at the interface, on a typical $(111)_{fcc}$ ledge. **d**, Atomic displacement component along $[1\bar{1}1]_{bcc}$ at the interface, on a typical $(111)_{fcc}$ ledge.

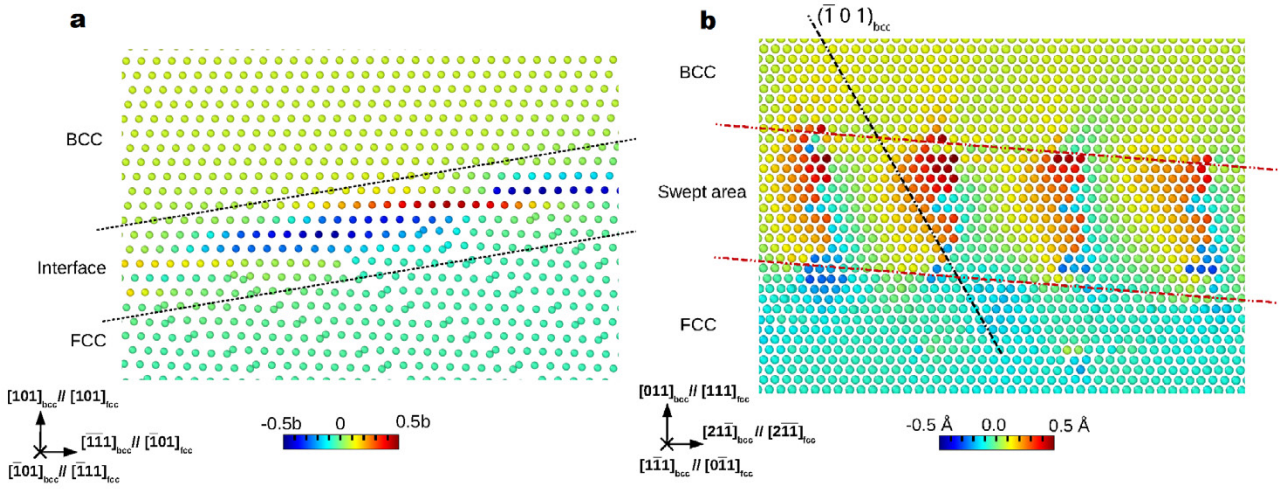


**Figure H.2 | Atomic displacements on $(\bar{1}01)_{bcc}$ plane. a**, Atomic displacements at the interface along $[1\bar{1}1]_{bcc}$, viewed on $(\bar{1}01)_{bcc}$ plane. **b**, Atomic displacements along Z ∥ $(232)_{fcc}$ viewed along the $[1\bar{1}1]_{bcc}$ direction. The non-homogeneous part relates to the domain swept by the interface (between the two dashed red traces). In this region, displacements are approximately constant along the $(\bar{1}01)_{bcc}$ plane, which is therefore the slip plane.

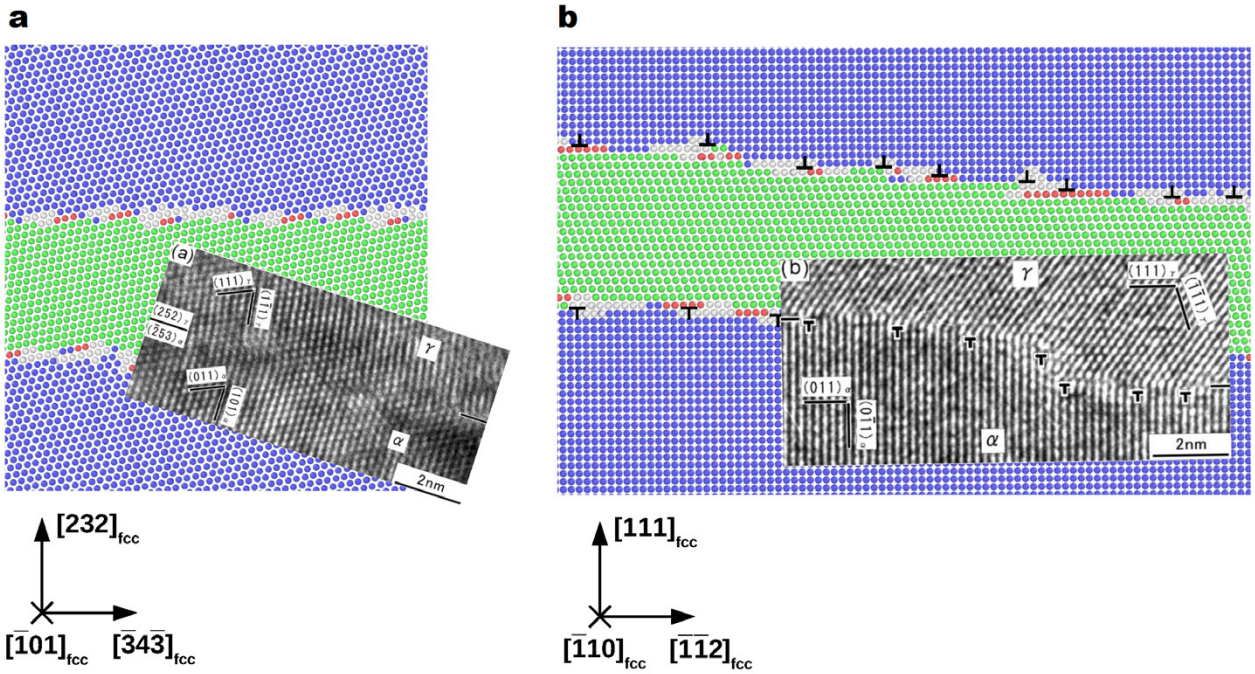


**Figure J.1 | Comparison between simulated interface and the ferritic bainite-austenite interface in bainite. a**, View along $[\bar{1}01]_{fcc}$. **b**, View along $[\bar{1}10]_{fcc}$. The micrographs from Ref. 4 are reproduced with the permission from Elsevier.